

**The Search for Higgs Boson Production in Association
with a Top-Quark Pair in pp Collisions at $\sqrt{s} = 8$ TeV in
the Lepton Plus Jets Final State**

John Garland Wood
Charlottesville, VA

B.S., The University of California, Berkeley, 2008

A Dissertation presented to the Graduate Faculty
of the University of Virginia in Candidacy for the Degree of
Doctor of Philosophy

Department of Physics

University of Virginia
May, 2015

Abstract

The most important goal of the Large Hadron Collider (LHC) is to elucidate the mechanism of electroweak symmetry breaking. The Standard Model (SM) Higgs boson is thought to be a prime candidate for this. The newly discovered boson announced on July 4th, 2012, with a mass of ~ 125 GeV/c 2 , has so far been shown to be consistent with a SM Higgs. However, the final confirmation of this new particle as the SM Higgs depends on subsequent measurements of all of its properties. The observation of this new particle in association with top-quark pairs would allow the couplings of this particle to top and bottom quarks to be directly measured. $t\bar{t}H$, with Higgs decaying to $b\bar{b}$ is an excellent channel to explore due to the dominant branching ratio of Higgs to $b\bar{b}$ and the kinematic handle the $t\bar{t}$ system offers on the event. However, it presents a plethora of difficult challenges due to a low signal to background ratio and uncertainties on kinematically similar SM backgrounds. This work discusses the search for Higgs boson production in association with a top-quark pair in pp collisions at $\sqrt{s} = 8$ TeV, collected by the Compact Muon Solenoid (CMS) experiment at the LHC. The search has been performed and published in two stages. The first analysis used the first 5.1 fb $^{-1}$, and was followed up by the second analysis with the full 2012 dataset, using a total integrated luminosity of 19.5 fb $^{-1}$

We approve the dissertation of John Garland Wood.

Date of Signature

Supervisor: Dr. Christopher Neu

Committee Chair: Dr. Bradley Cox

Committee Member: Dr. Hank Thacker

PhD Committee Chair: Dr. Astronomy Person

Contents

Contents	iv
List of Figures	vi
List of Tables	viii
1 Introduction	1
2 Theoretical Background	4
2.1 An Overview of Quantum Field Theory	4
2.2 Abelian Gauge Theories of Particle Interactions	7
2.3 Non-Abelian Gauge Theories of Particle Interactions	9
2.4 The Higgs Mechanism in an Abelian Theory	12
2.5 The Higgs Mechanism in a non-Abelian Theory	14
2.6 Glashow Weinberg Salam Theory	16
2.7 The Standard Model of Particle Physics	22
2.8 Higgs Production in pp Collisions at the LHC	24
2.9 $t\bar{t}H$ Production in pp Collisions at the LHC	26
2.10 Background Processes to $t\bar{t}H$	27
2.11 Potential BSM Effects on $t\bar{t}H$ production	30
3 The Large Hadron Collider	32
3.1 The LHC Accelerator Complex	34
3.2 LHC Magnets	42
3.3 LHC RF Technology	48
3.4 The LHC Cryogen System	51
3.5 The LHC Vacuum System	52
4 The Compact Muon Solenoid	54
4.1 The Inner Tracker	54

4.2	The Electromagnetic Calorimeter	54
4.2.1	Vacuum Photo-Triodes	54
4.2.2	Test Rig at UVa	54
4.2.3	Results of UVa Tests	54
4.3	The Hadronic Calorimeter	54
4.4	Forward Calorimetry	55
4.5	Magnet and Return Yoke	55
4.6	Muon Chambers	55
4.7	Data Collection Overview	55
5	Particle Reconstruction at CMS	56
5.1	Muon Reconstruction	56
5.2	Electron Reconstruction	56
5.3	Photon Reconstruction	56
5.4	Jet Reconstruction	56
5.5	Tau Reconstruction	57
5.6	Missing Transverse Energy Reconstruction	57
	Bibliography	58
	List of Acronyms	64

List of Figures

1.1	The CMS experiment has observed a new boson at $m \sim 125 \text{ GeV}/c^2$	1
1.2	A Feynman diagram of the $t\bar{t}H$ process, with $\text{Higgs} \rightarrow b\bar{b}$, and the $t\bar{t}$ -system decaying semi-leptonically	3
2.1	Leading and Next to Leading Order Feynman diagrams for the coulomb scattering process	6
2.2	The global average of α_s , the QCD coupling constant.	7
2.3	A visual representation of the Higgs potential	12
2.4	Experimental milestones of the Standard Model	23
2.5	Higgs production cross-sections at the LHC, for 7-14 TeV pp collisions	24
2.6	Feynman diagrams for the three largest Higgs production modes at the LHC . .	25
2.7	Feynman diagram for $t\bar{t}H$ production	26
2.8	Feynman diagrams for the semileptonic $t\bar{t}H$ process and its irreducible background, $t\bar{t} + b\bar{b}$	27
2.9	Feynman diagrams for the $t\bar{t}W$ and $t\bar{t}Z$ background processes	28
2.10	Feynman diagrams for the single t , s,t , and tW background processes	28
2.11	Feynman diagrams for the W, Z plus jets, and diBoson (WW, WZ, ZZ) production. .	29
2.12	Measurements of $t\bar{t}H$ backgrounds at CMS	29
2.13	The cancellation of the divergent Higgs mass from a loop of top-quarks is cancelled by a loop of supersymmetric top-quarks, stop-quarks,	31
3.1	Aerial view of the LHC complex, spanning the French-Swiss border [1]	32
3.2	Integrated Luminosity delived to the CMS experiment from 2010-12	34
3.3	The LHC accelerator complex, taking protons from a bottle of Hydrogen at the Linac2, all the way to the LHC ring	35
3.4	Features of the Linac2, the first stage of acceleration in the LHC injection chain .	36
3.5	Features of the PS booster, the second stage of the LHC injection chain	37
3.6	Features of the PS, the third stage of the LHC injection chain	40

3.7	Features of the SPS, the fourth and final stage of the LHC injection chain	41
3.8	The LHC ring is divided into eight octants	43
3.9	The single turn injection scheme. A septum magnet makes the initial alignment. The kicker magnet times the injection and makes the final alignment. Bumper magnets align the LHC beam with the injected beam.	44
3.10	Layout of Interaction Region 8, where one proton beam is injected into the LHC ring. A transfer line from the SPS bring a proton in from the right. In green, a septum magnet aligns the beam horizontally with the LHC. In blue, a kicker magnet makes the final vertical alignment into the LHC, and is timed to fill one of the 400 MHz buckets of the RF capture system	44
3.11	The initial filling of 6 batches of protons from the PSB to the PS, leaves 12 empty buckets in the PS bunch structure. The rise time of the SPS magnet creates an additonal gap in the SPS bunch structure. Additional gaps emerge due to the rise time of the LHC injection and dumping kicker magnets	45
3.12	Features of the dipole magnets used in the LHC	46
3.13	Features of the dipole magnets used in the LHC	47
3.14	Features of the 400 MHz superconducting RF system used in the LHC	48
3.15	A klystron uses a weak RF signal coupled to a resonace cavity to bunch an electron beam, which in turn creates an amplified RF signal as it passes through a second resonance cavity tuned to the same frequency.	49
3.16	One of sixteen 300 kW, 400 MHz klystrons that power the superconducting RF cavities that accelerate the proton beam.	50
3.17	Layout of the five cryogenic islands, which are home to the eight facilities that provide liquid helium to the LHC	51
3.18	Features of the 4.5 K refridgeration system	51
3.19	Cross section schematic of the cryogenic distribution system in the LHC tunnel .	52
3.20	Beam screen for the LHC, with slits to allow for easy pumping of residual gas molecules in the beampipe.	53

List of Tables

2.1 The quantum numbers Isospin and Hypercharge are assigned for each of the $SU(2)$ and $U(1)$ symmetries respectively	20
---	----

¹ Chapter 1

² Introduction

³ On July 4th, 2012, the Compact Muon Solenoid (CMS) and A Toroidal LHC Apparatus (ATLAS)
⁴ experiments announced the discovery of a new boson of mass $\sim 125 \text{ GeV}/c^2$ [2] [3]. The particle
⁵ has been shown to be increasingly consistent with the description of the boson predicted by the
⁶ Higgs mechanism of the SM, as measurements on its mass, width, and quantum numbers are
⁷ completed. However, there are several properties of this new boson, which remain to be tested.
⁸ Figure 1.1 shows a consistent mass peak between the $H \rightarrow ZZ$ and $H \rightarrow \gamma\gamma$ channels at the
⁹ CMS experiment.

¹⁰ The Yukawa coupling of the Higgs boson to the top-quark in the SM is the largest coupling
¹¹ among the fundamental particles and is well predicted - thus offering an excellent test of the
¹² nature of the coupling of the Higgs to fermions, as well as a potential probe into physics Beyond
¹³ the Standard Model (BSM) that would alter this value from the SM prediction. The production
¹⁴ of the Higgs boson in association with top-quark pairs is the best production mode at the LHC
¹⁵ that offers direct access to the top-Higgs coupling. The dominant production mode of Higgs
¹⁶ at the LHC, gluon-gluon fusion, involves a triangle loop of strongly-coupled fermions, which

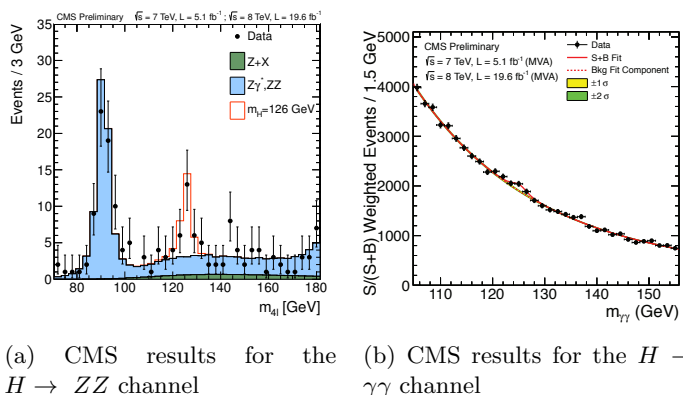


Figure 1.1: The CMS experiment has observed a new boson at $m \sim 125 \text{ GeV}/c^2$

¹⁷ includes all of the other quarks, as well as the potential for BSM particles.

¹⁸ $t\bar{t}H$ production also has the ability to constrain some extensions of the SM that would not
¹⁹ modify the Higgs branching fractions enough to be seen within current experimental precision.
²⁰ Such models include Little Higgs models, models with extra dimensions, top-color models, and
²¹ composite Higgs models that introduce a vector-like top partner, a t' , that can decay to tH ,
²² bW , or tZ states. Both $t't'$ and $t't$ production would produce a $t\bar{t}H$ final state, or one that is
²³ indistinguishable from it ($tHbW$). Upper limits on $t\bar{t}H$ production would also provide limits on
²⁴ the previously described models, which would be complementary to existing direct searches for
²⁵ t' particles, which attempt to reconstruct the t' resonance.

²⁶ The $t\bar{t}H$ channel has a rich set of possible final states. Each top-quark will decay to a b -
²⁷ quark and a W boson. The W boson will subsequently decay to two quarks, or a lepton and a
²⁸ neutrino. These decays are classified as either hadronic, semi-leptonic, or di-leptonic for zero,
²⁹ one, or both t quarks decaying leptonically respectively. The Higgs may decay to b -quark, W ,
³⁰ Z , τ , or γ pairs. In fact, this is one of the only production modes at the LHC which has access
³¹ to every Higgs decay mode, as other production mechanisms are swamped by large backgrounds
³² preventing measurements of all Higgs decay types.

³³ The search is performed with the CMS experiment, a modern, general purpose particle
³⁴ detector capable of reconstructing and identifying hadronic jets, photons, electrons, muons,
³⁵ and tau leptons. The hermetic design, and its high precision and efficiency in reconstructing
³⁶ and tracking every particle in a pp collision, also makes it suitable for reconstructing missing
³⁷ transverse energy from the calculated momentum imbalance of all of the measured particles in
³⁸ the event. This missing transverse energy is often the signature of a neutrino, which is the
³⁹ only SM particle capable of escaping detection. The detector uses a 3.8 T axial magnetic field,
⁴⁰ produced by the solenoid it is named after, to bend charged particles as they travel through
⁴¹ the detector. The measured curvature of their tracks allows the momentum of the particles to
⁴² be calculated with to a high precision. Tracks are formed and particles are reconstructed by a
⁴³ combination of sub-detector systems which work together to form the final reconstructed
⁴⁴ image of each particle in the collision.

⁴⁵ This thesis will focus on a semi-leptonic decay of the top-quarks, with the Higgs decaying to
⁴⁶ a b -quark pair. Figure 1.2 is Feynman diagram of the $t\bar{t}H$ process. The largest background to
⁴⁷ this process is top-quark pair production with extra jets originating from Initial State Radiation
⁴⁸ (ISR) or Final State Radiation (FSR) radiation, $t\bar{t} + jets$. The irreducible background is formed
⁴⁹ by top-quark pairs, where a gluon is radiated and decays to b -quark pairs, $t\bar{t} + b\bar{b}$. In addition
⁵⁰ to the large backgrounds, the high jet multiplicity in the $t\bar{t}H$ final state gives rise to a combina-
⁵¹ torics problem in associating each jet with its role in the $t\bar{t}H$ system. This inevitably leads to

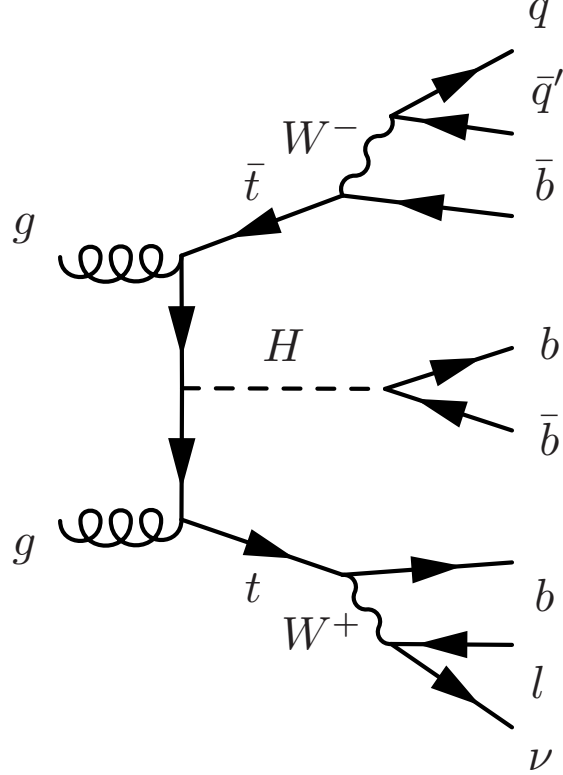


Figure 1.2: A Feynman diagram of the $t\bar{t}H$ process, with $H \rightarrow b\bar{b}$, and the $t\bar{t}$ -system decaying semi-leptonically

misidentifying which jets are the decay product of the Higgs, and thus additionally smears out the resolution on the mass of the Higgs. Due to the similarity of the $t\bar{t} + b\bar{b}$ background and the combinatorics issue, no single variable is suitable for signal extraction. A Multi-Variate Analysis (MVA) technique is used in an attempt to isolate the $t\bar{t}H$ signal from the $t\bar{t} + jets$ background. The MVA provides a one-dimensional discriminant based on several input variables related to the kinematics of the event. This discriminant is then used to perform signal extraction and set upper-limits on $t\bar{t}H$ production. The results of two searches will be presented. The first result used the first 5.1 fb^{-1} of the 2012 dataset, with center of mass energy of 8 TeV, and was published in the Journal of High Energy Physics (JHEP), May 2013. The second result was updated with the full 19.4 fb^{-1} 8 TeV dataset, and was published in JHEP, September 2014.

⁶² Chapter 2

⁶³ Theoretical Background

⁶⁴ The Standard Model (SM) of particle physics represents the sum of knowledge of the fundamen-
⁶⁵ tal particles and their interactions with each other. It is a Quantum Field Theory (QFT) that
⁶⁶ represents the interactions of each of the fundamental forces through the symmetry of a mathe-
⁶⁷ matical object known as a Lie group. It is the theory that dictates the rate that the $t\bar{t}H$ process
⁶⁸ is produced, as well as the kinematics of every particle involved. As such, its predictions are
⁶⁹ critical for modeling the characteristic signature of the $t\bar{t}H$ signal in the CMS detector, as well as
⁷⁰ the background processes, like $t\bar{t} + b\bar{b}$ which leave a kinematically similar final state signature.

⁷¹ 2.1 An Overview of Quantum Field Theory

⁷² Quantum Field Theory (QFT) was developed out of the need for a relativistic description of
⁷³ quantum mechanics. Since the Einstein relation $E = mc^2$ allows for the creation of particle-
⁷⁴ antiparticle pairs, the single-particle description used in non-relativistic quantum mechanics,
⁷⁵ fails describe this phenomenon [4]. This additionally fails when considering that Heisenberg's
⁷⁶ uncertainty relation, $\Delta E \cdot \Delta t = \hbar$, allows for an arbitrary number of intermediate, virtual
⁷⁷ particles to be created. By quantizing a field representing a certain type of particle, multiparticle
⁷⁸ states are naturally described as discrete excitations of that field.

⁷⁹ Lorentz invariance, and the need to preserve causality, also define a fundamental relationship
⁸⁰ between matter and antimatter. The propagation of a particle across a space-like interval is
⁸¹ treated equivalently to the an anti-particle propagating in the opposite direction [4]. This is
⁸² done so that the net probability amplitude for the particles to have an effect on a measurement
⁸³ occurring across a space-like interval cancel each other, thus preserving causality. This cancel-
⁸⁴ lation requirement additionally implies that the particle and anti-particle have the same mass,
⁸⁵ with opposite quantum numbers such as spin or electric charge.

86 The Lorentz transformations for a scalar field are different than for a field with internal de-
 87 grees of freedom, such as spin. A rotation on a vector field, will affect both its location, as well
 88 as it's orientation [4]. This means the Lorentz invariant equation of motion describring a scalar
 89 field will have a different form than equations of motion for a field with spin. The most relevant
 90 equations describe the particles of SM, which contain spins of 0, 1/2, and 1. They are described
 91 by the Klein-Gordan, Dirac, and Proca equations respectively.

92

Klein-Gordon equation, for scalar (spin 0) fields

$$(\partial^2 + m^2)\phi = 0 \quad (2.1)$$

Dirac equation, for spinor (spin 1/2) fields

$$(i\gamma^\mu \partial_\mu - m)\psi = 0 \quad (2.2)$$

Proca equation, for vector (spin 1) fields

$$\partial_\mu(\partial^\mu A^\nu - \partial^\nu A^\mu) + m^2 A^\nu = 0 \quad (2.3)$$

93 With these equations, one can build a theory of free particles. The Lagrangian formulation is
 94 the most appropriate since all expressions are explicitly Lorentz invariant [4]. The Lagrangians
 95 for the Klein-Gordon, Dirac, and Proca equations are given as:

96

Klein-Gordon Lagrangian, for real and complex scalar fields

$$\begin{aligned} \mathcal{L} &= \partial_\mu \partial^\mu \phi^2 - \frac{1}{2} m^2 \phi^2 \\ \mathcal{L} &= (\partial_\mu \phi)^*(\partial^\mu \phi) - m^2 (\phi)^*(\phi) \end{aligned} \quad (2.4)$$

Dirac Lagrangian, for spinor fields

$$\mathcal{L} = i\bar{\psi} \gamma^\mu \partial_\mu \psi - m\bar{\psi} \psi \quad (2.5)$$

Proca Lagrangian, for vector fields

$$\mathcal{L} = -\frac{1}{4} F_{\mu\nu} F^{\mu\nu} + m^2 A^\nu A_\nu \quad (2.6)$$

97 where $F_{\mu\nu}$, is the field strength tensor, defined as $F_{\mu\nu} = \partial_\mu A_\nu - \partial_\nu A_\mu$

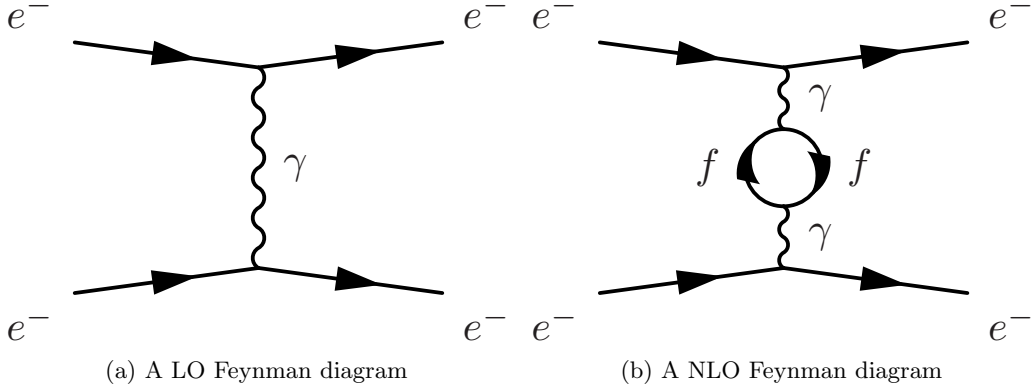


Figure 2.1: Leading and Next to Leading Order Feynman diagrams for the coulomb scattering process

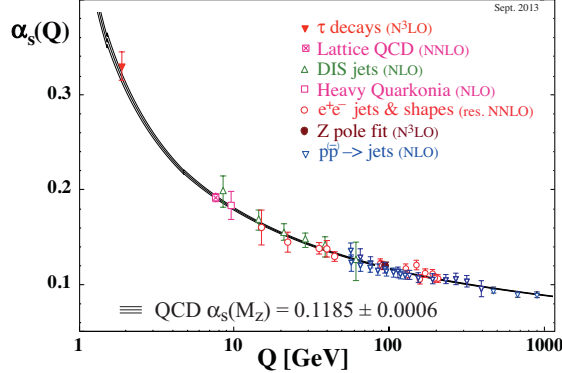
98 Interactions are generated by coupling multiple fields together in a single term, such as
 99 $ieA_\mu\bar{\psi}\psi$ and treating it as a perturbation to the free field theory. This implies every interaction
 100 between particles is carried out by a virtual mediating particle. When two electrons scatter off
 101 one another, they are really exchanging a virtual photon, the mediator of the electromagnetic
 102 force. The W^\pm and Z bosons mediate the weak force, while the *gluons* mediate the strong force.

$$\mathcal{L} = \mathcal{L}_{Free} + \mathcal{L}_{Interacting} \quad (2.7)$$

103 In order to calculate the probability and dynamics of two particles interacting with one
 104 another, an integral, constrained by energy and momentum conservation, over the phase space
 105 of outgoing particles and the scattering amplitude, \mathcal{M} , is evaluated. The scattering amplitude is
 106 calculated by using the propagator (Green's function of the free particle theory) for the incoming,
 107 mediating, and outgoing particles, with an appropriate weighting function, or vertex factor,
 108 for each point the particles interact in the scattering process, and then integrating over the
 109 momentum of the mediating particle. Richard Feynmann developed a set of rules for the writing
 110 down the propagators and vertex factors directly from the Lagrangian, and easily computing the
 111 scattering amplitude. He also introduced an elegant pictographic notation useful for visualizing
 112 particle interactions, known as Feynmann diagrams.

113 With these tools, one can calculate the probability amplitudes of a given process occurring
 114 to Leading Order (LO) without any difficulties. However, when calculations in Next to Leading
 115 Order (NLO) are performed, and loop diagrams of virtual particles are considered, the probability
 116 amplitudes associated with a given process diverge to infinity. This occurs when one integrates
 117 over all of the possible momentum allowed by intermediate, loops of virtual particles, which due
 118 to Heisenberg's uncertainty principle, are allowed to take on any value of momentum. Figure
 119 2.1 shows an example of a LO and NLO process.

120 The systematic removal of divergences from a theory is called renormalization. The di-

Figure 2.2: The global average of α_s , the QCD coupling constant.

vergences are absorbed into the definitions of the free parameters of the theory, making the parameters a function of the energy scale the process occurs at, instead of a constant. This allows for the calculations of fundamental processes to completed, as long as the energy scale of the interaction is known. A modern interpretation of renormalization was provided by Kenneth Wilson [5] [6]. Instead of seeing the effects of high momentum calculations after moving to NLO in perturbation theory, one uses an effective Lagrangian, computed by integrating out shells of momentum beginning at the energy cutoff of the theory, where the NLO effects begin the dominate. The dimensions of integration are then rescaled and the result of evaluating the integral over the momentum shell is absorbed into the definition of free parameters. The processes is iterated until the energy scale of the interaction is reached. The functional dependence of the parameters is then directly present in the resulting effective Lagrangian, instead of appearing suddenly when accounting for the one-loop contributions at NLO. Regardless of how strange this procedure seem, the running of the coupling constant as a function of interaction engergy has been validated experimentally time and time and again, as shown in Figure 2.2 [7].

2.2 Abelian Gauge Theories of Particle Interactions

In 1930, Herman Weyl introduced the idea that the interactions between fields can be generated by requiring them to be invariant under guage tansformations of a local symmetry [8]. For electromagnetism, the local symmetry is that of the Lie group, $U(1)$. It is an abelian group, which has the property that the generators of the group symmetry commutes with themselves. The $U(1)$ symmetry is invariant under phase rotations. By requiring local guage invariance, the Lagrangian must be unchanged under the

$$\psi(x) \rightarrow e^{i\alpha(x)}\psi(x). \quad (2.8)$$

¹⁴² Consider the Lagrangian for a free spin 1/2 particle:

$$\mathcal{L} = \bar{\psi}(i\gamma^\mu \partial_\mu - m)\psi \quad (2.9)$$

¹⁴³ The first term in the Lagrangian, involving the derivative, acts on $\alpha(x)$, creating a new term in
¹⁴⁴ the Lagrangian, breaking its invariance under the local phase transformation.

$$\mathcal{L} \rightarrow \mathcal{L} - (\partial_\mu \alpha) \bar{\psi} \gamma^\mu \psi \quad (2.10)$$

¹⁴⁵ Thus, a new term must be added to the original Lagrangian to cancel out the term arising from
¹⁴⁶ the local phase transformation. This is achieved by defining the covariant derivative:

$$D_\mu = \partial_\mu + ieA_\mu \quad (2.11)$$

¹⁴⁷ where A_μ is a new vector field that transforms as follows:

$$A_\mu(x) \rightarrow A_\mu(x) - \frac{1}{e}\partial_\mu \alpha(x) \quad (2.12)$$

¹⁴⁸ The covariant derivative thus transforms like

$$\begin{aligned} D_\mu \psi(x) &\rightarrow [\partial_\mu + ie(A_\mu - \frac{1}{e}\partial_\mu \alpha)] e^{i\alpha(x)} D_\mu \psi(x) \\ &= e^{i\alpha(x)} [\partial_\mu + ie(A_\mu - \frac{1}{e}\partial_\mu \alpha + \frac{1}{e}\partial_\mu \alpha)] D_\mu \psi(x) \\ &= e^{i\alpha(x)} (\partial_\mu + ieA_\mu) \psi(x) \\ &= e^{i\alpha(x)} D_\mu \psi(x) \end{aligned} \quad (2.13)$$

¹⁴⁹ This covariant derivative transforms in the same way that $\psi(x)$ does, and the new locally gauge
¹⁵⁰ invariant Lagrangian becomes

$$\begin{aligned} \mathcal{L} &= \bar{\psi}(i\gamma^\mu D_\mu - m)\psi - \frac{1}{4}F^{\mu\nu}F_{\mu\nu} \\ &= i\bar{\psi}\gamma^\mu \partial_\mu \psi - \bar{\psi}\gamma^\mu \psi A_{\mu u} - m\bar{\psi}\psi - \frac{1}{4}F^{\mu\nu}F_{\mu\nu} \end{aligned} \quad (2.14)$$

¹⁵¹ where

$$F^{\mu\nu} = (\partial^\mu A^\nu - \partial^\nu A^\mu) \quad (2.15)$$

¹⁵² and $\frac{1}{4}F^{\mu\nu}F_{\mu\nu}$ is the kinetic energy term of the Proca equation for the new vector field.

¹⁵³ This new Lagrangian is identical to the QED Lagrangian, except it was derived beginning
¹⁵⁴ with a free Dirac theory and requiring the field to be locally gauge invariant under $U(1)$ transfor-
¹⁵⁵ mations. This necessitated the introduction of a new vector field, A_μ , as well as an interaction

¹⁵⁶ term with it. This implies that the electromagnetic force can be represented by the requirement
¹⁵⁷ of local $U(1)$ symmetry on a free Dirac particle.

¹⁵⁸ It should be noted, that if the photon had mass, an additional term from the Proca equation
¹⁵⁹ would have to be added to the Lagrangian, $m^2 A_\mu A^\mu$. This term complicates the picture since
¹⁶⁰ it is not invariant under local phase transformations, and cannot be compensated for through a
¹⁶¹ different choice of A_μ . This implies that the bosons of a gauge theory must be massless in order
¹⁶² to preserve local gauge invariance.

¹⁶³ 2.3 Non-Abelian Gauge Theories of Particle Interactions

¹⁶⁴ In 1954, Yang and Mills worked to extend this idea to symmetries of different gauge groups [9].
¹⁶⁵ Their most important accomplishment was developing this procedure for non-abelian groups.
¹⁶⁶ These are groups, where the transformation does not involve a simple variable $\alpha(x)$, but rather an
¹⁶⁷ entire matrix of dimension $n > 2$. These matrices do not commute with each other, and their work
¹⁶⁸ developed the procedure for applying local gauge invariance described above to the more complex,
¹⁶⁹ higher dimensional symmetries, such as $SU(2)$ and $SU(3)$. Consider the case of $SU(2)$ symmetry.
¹⁷⁰ The theory is appropriate for describing the dynamics of two fermion fields, represented as a
¹⁷¹ doublet:

$$\psi = \begin{pmatrix} \psi_1(x) \\ \psi_2(x) \end{pmatrix} \quad (2.16)$$

¹⁷² this will transform under the $SU(2)$ transformation as a two-component spinor:

$$\psi \rightarrow \exp\left(i\alpha^i \frac{\sigma_i}{2}\right) \psi \quad (2.17)$$

¹⁷³ where σ^i are the Pauli matrices:

$$\sigma^1 = \begin{pmatrix} 0 & 1 \\ 1 & 0 \end{pmatrix}, \sigma^2 = \begin{pmatrix} 0 & -i \\ i & 0 \end{pmatrix}, \sigma^3 = \begin{pmatrix} 1 & 0 \\ 0 & -1 \end{pmatrix} \quad (2.18)$$

¹⁷⁴ and have the commutation relation defined by:

$$\left[\frac{\sigma^i}{2}, \frac{\sigma^j}{2} \right] = i\epsilon^{ijk} \frac{\sigma^k}{2} \quad (2.19)$$

¹⁷⁵ Similar to the case of the $U(1)$ Abelian symmetry, in order to form a lagrangian that is locally
¹⁷⁶ gauge invariant, three vector fields, A_μ^i , $i = 1, 2, 3$, are introduced, and coupled to ψ through the
¹⁷⁷ covariant derivative:

$$D_\mu = (\partial_\mu - igA_\mu^i \frac{\sigma^i}{2}) \quad (2.20)$$

¹⁷⁸ to ensure that the derivative covaries with the transformation, the fields, A_μ^i will transform like:

$$A_\mu^i \frac{\sigma^i}{2} \rightarrow A_\mu^i \frac{\sigma^i}{2} + \frac{1}{g}(\partial_\mu \alpha^i) \frac{\sigma^i}{2} + i \left[\frac{\alpha^i \sigma^i}{2}, A_\mu^i \frac{\sigma^i}{2} \right] \quad (2.21)$$

¹⁷⁹ The third term, which was absent from the abelian form of the transformation, is necessary to
¹⁸⁰ account for the non-commutation of the pauli matrices. This non-communtation also changes
¹⁸¹ the form of the field strength tensor, $F_{\mu\nu}^i$:

$$F_{\mu\nu}^i = \partial_\mu A_\nu^i - \partial_\nu A_\mu^i + g\epsilon^{ijk} A_\mu^j A_\nu^k \quad (2.22)$$

¹⁸² The entire $SU(2)$ invariant Lagrangian can then be written as:

$$\begin{aligned} \mathcal{L}_{Yang-Mills} &= -\frac{1}{4}F_{\mu\nu}^i F^{i\mu\nu} + \bar{\psi}(i\gamma^\mu D_\mu)\psi \\ &= -\frac{1}{4}F_{\mu\nu}^i F^{i\mu\nu} + \bar{\psi}(i\gamma^\mu \partial_\mu - igA_\mu^i \frac{\sigma^i}{2})\psi \end{aligned} \quad (2.23)$$

¹⁸³ This procedure generalizes to any continuous group of symmetries. The basic steps involve
¹⁸⁴ idenitifying the generators of the transformation:

$$\psi(x) \rightarrow e^{i\alpha^a t^a} \psi \quad (2.24)$$

¹⁸⁵ where t^a are a set of matrices with the commutation relationship:

$$[t^a, t^b] = if^{abc}t^c \quad (2.25)$$

¹⁸⁶ where f^{abc} is the structure constant for the goup. The covariant derivative is then defined as:

$$D_\mu = \partial_\mu - igA_\mu^a t^a \quad (2.26)$$

¹⁸⁷ where the fields, A_μ^a , transform like:

$$A_\mu^a \rightarrow A_\mu^a + \frac{1}{g}\partial_\mu \alpha^a + f^{abc}A_\mu^b \alpha^c \quad (2.27)$$

¹⁸⁸ the field strength tensor is then formed as:

$$F_{\mu\nu}^a = \partial_\mu A_\nu^a - \partial_\nu A_\mu^a + f^{abc} A_\mu^b A_\nu^c \quad (2.28)$$

¹⁸⁹ and finally, the locally, gauge invariant Lagrangian will have the form:

$$\begin{aligned}\mathcal{L}_{\text{General, non-Abelian}} &= -\frac{1}{4}F_{\mu\nu}^a F^{a\mu\nu} + \bar{\psi}(i\gamma^\mu D_\mu)\psi \\ &= -\frac{1}{4}F_{\mu\nu}^a F^{a\mu\nu} + \bar{\psi}(i\gamma^\mu \partial_\mu - ig A_\mu^a t^a)\psi\end{aligned}\quad (2.29)$$

190 In 1964, Murray Gell-Mann and Zweig independently developed a model of hadron interactions,
 191 that described the spectrum of baryons and mesons in terms of combinations of fundamental
 192 particles, which Gell-Mann named quarks [10] [11] [12]. In their model, three quarks: u, d, s
 193 formed an $SU(3)$ flavor symmetry. However, this did not explain the appearance of only two and
 194 three quark combinations, the mesons and baryons. It also could not explain the spin statistics
 195 of the baryons. The Δ^{++} , Δ^- , and Ω^- , particles all have uuu , ddd , sss quark combinations,
 196 respectively, with their spins aligned. That is to say, these baryons seem to violate the Pauli-
 197 exclusion principle since all three quarks seem to occupy the same quantum state simultaneously.

198 In 1964, O.W. Greenberg solved this problem by proposing that quarks also have an additional
 199 quantum number, *color*, that come in three types: red, green, blue [13]. The requirement that
 200 all stable hadrons be color neutral: either possessing equal amounts of all three colors in qqq
 201 combinations, or a $q\bar{q}$ pair sharing the same color, also explained the observation of only 2 and
 202 3 quark combinations in experiments. These three colors form an $SU(3)$ symmetry, and is the
 203 gauge symmetry describing the interactions of quarks and leptons. This theory is known as
 204 Quantum Chromodynamics (QCD). Its derivation follows from the procedure outlined above.
 205 This group has eight generators, known as the Gell-Mann matrices, and are defined as:

$$\begin{aligned}t^1 &= \frac{1}{2} \begin{pmatrix} 0 & 1 & 0 \\ 1 & 0 & 0 \\ 0 & 0 & 0 \end{pmatrix}, \quad t^2 = \frac{1}{2} \begin{pmatrix} 0 & -i & 0 \\ i & 0 & 0 \\ 0 & 0 & 0 \end{pmatrix}, \quad t^3 = \frac{1}{2} \begin{pmatrix} 1 & 0 & 0 \\ 0 & -1 & 0 \\ 0 & 0 & 0 \end{pmatrix} \\ t^4 &= \frac{1}{2} \begin{pmatrix} 0 & 0 & 1 \\ 0 & 0 & 0 \\ 1 & 0 & 0 \end{pmatrix}, \quad t^5 = \frac{1}{2} \begin{pmatrix} 0 & 0 & -i \\ 0 & 0 & 0 \\ i & 0 & 0 \end{pmatrix} \\ , \quad t^6 &= \frac{1}{2} \begin{pmatrix} 0 & 0 & 0 \\ 0 & 0 & 1 \\ 0 & 1 & 0 \end{pmatrix}, \quad t^7 = \frac{1}{2} \begin{pmatrix} 0 & 0 & 0 \\ 0 & 0 & -i \\ 0 & -i & 0 \end{pmatrix}, \quad t^8 = \frac{1}{2\sqrt{3}} \begin{pmatrix} 1 & 0 & 0 \\ 0 & 1 & 0 \\ 0 & 0 & -2 \end{pmatrix}\end{aligned}\quad (2.30)$$

206 and a Lagrangian defined as:

$$\begin{aligned}\mathcal{L}_{QCD} &= -\frac{1}{4}G_{\mu\nu}^a G^{a\mu\nu} + \bar{\psi}(i\gamma^\mu D_\mu)\psi \\ &= -\frac{1}{4}G_{\mu\nu}^a G^{a\mu\nu} + \bar{\psi}(i\gamma^\mu \partial_\mu - ig A_\mu^a t^a)\psi\end{aligned}\quad (2.31)$$

207 where t^a are the Gell-Mann matrices defined in equation 2.30 and the fields A_μ^a are the eight
 208 mediators of the QCD force, the *gluons*.

209 Like all non-abelian guage theories, it is asymptotically free. Thus, the strength of the cou-
 210 pling constant, α_s , decreases as the momentum-transfer, Q in interaction increases. This allows
 211 the use of perturbation theory for high-momentum calculations, therefore allowing calculations
 212 of hadronic-processes for experimental evaluation.

The idea of local gauge invariance was successful in describing the dynamics of QED and QCD, which only contain massless gauge bosons. Theorists had long postulated that the weak force was so weak because it was being facilitated by massive bosons, but adding a mass term for a boson breaks the local gauge invariance. So, a tool was needed to reconcile the concept of local gauge invariance, which works so well for the other forces, with the prospect of the weak force being facilitated by massive gauge bosons.

2.4 The Higgs Mechanism in an Abelian Theory

In 1964 Peter Higgs introduced the idea that the gauge bosons can acquire their mass through the breaking of an underlying symmetry [14]. In other words, the natural symmetry of the Lagrangian describing a particular interaction could be different than the symmetry we observe in nature. Consider an abelian example of complex scalar field theory, coupled to itself and to an electromagnetic field [4].

$$\mathcal{L} = -\frac{1}{4}(F_{\mu\nu})^2 + |D_\mu\phi|^2 - V(\phi) \quad (2.32)$$

where $D_\mu = \partial_\mu + ieA_\mu$, is the familiar covariant derivative, and the Lagrangian is invariant under the $U(1)$ transformation as described earlier. The potential term, $V(\phi)$ has the form

$$V(\phi) = -\mu^2\phi^*\phi + \frac{\lambda}{2}(\phi^*\phi)^2 \quad (2.33)$$

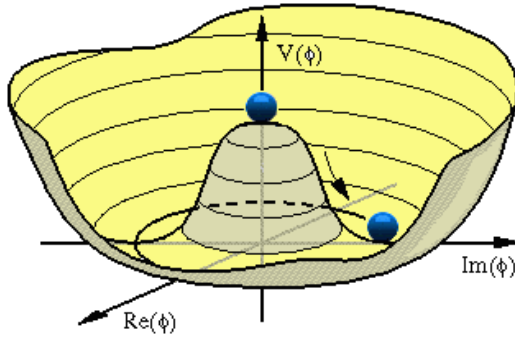


Figure 2.3: A visual representation of the Higgs potential

if $\mu^2 > 0$ the shape of the potential no longer has a minimum at $\langle\phi\rangle = 0$. Figure 2.3 shows a plot of the potential energy of ϕ in terms of each of its components. The new minimum potential energy occurs at:

$$\langle\phi\rangle = \phi_0 = \left(\frac{\mu^2}{\lambda}\right)^{1/2} \quad (2.34)$$

and while the field has a ground state at the zero potential point it is in an unstable equilibrium. Any quantum fluctuation about this point will take the field into the lower energy configuration with a ground state about the new minimum. When the Langrangian is expanded about 2.34, the field, ϕ is rewritten as:

$$\phi(x) = \phi_0 + \frac{1}{\sqrt{2}}(\phi_1(x) + i\phi_2(x)) \quad (2.35)$$

the potential term, $V(x)$, then becomes:

$$V(x) = -\frac{1}{2\lambda}\mu^4 + \frac{1}{2} \cdot 2\mu^2\phi_1^2 + \mathcal{O}(\phi_i^3) \quad (2.36)$$

where we can notice that ϕ_1 has acquired a mass term with, $m = \sqrt{2}\mu$, while the scalar field ϕ_2 remains massless, and is known as the Goldstone boson. The covariant derivative is also transformed as:

$$|D_\mu\phi|^2 = \frac{1}{2}(\partial_\mu\phi_1)^2 + \frac{1}{2}(\partial_\mu\phi_2)^2 + \sqrt{2}e\phi_0 \cdot A_\mu\partial^\mu\phi_2 + e^2\phi_0^2A_\mu A^\mu + \dots \quad (2.37)$$

where cubic and quartic terms of A_μ , ϕ_1 , and ϕ_2 have been dropped. The important term is the last one, which can be interpreted as a mass term of the vector field, A_μ

$$\Delta\mathcal{L}_M = \frac{1}{2}m_A A_\mu A^\mu = e^2\phi_0^2 A_\mu A^\mu \quad (2.38)$$

where $m_A = 2e^2\phi_0^2$, has arisen from consequences of a non-zero vacuum expectation value of the ϕ field. The remaining, massless Godlstone boson, ϕ_2 is not a physical particle, but rather a consequence of the choice of guage. This is illustrated when we can use the $U(1)$ guage symmetry to rotate the field $\phi(x)$ such that the field disappears.

$$\begin{aligned} \phi &\rightarrow \phi' = e^{i\alpha}(\phi_1 + \phi_2) \\ &= (\cos\alpha + i\sin\alpha)(\phi_1 + \phi_2) \\ &= (\phi_1 \cos\alpha - \phi_2 \sin\alpha) + i(\phi_1 \sin\alpha + \phi_2 \cos\alpha) \\ &= (\phi_1 - \phi_2 \tan\alpha) + i(\phi_1 \tan\alpha + \phi_2) \end{aligned} \quad (2.39)$$

Choosing $\alpha = -\tan\phi_2/\phi_1$ will make ϕ' a real quantity and elminate it's imaginary component, ϕ'_2 . The lagrangian can then be rewritten in terms of the rotated field ϕ' and see that massless boson is indeed removed from the theory.

$$\begin{aligned}\mathcal{L} = & \frac{1}{2}(\partial_\mu\phi'_1)(\partial^\mu\phi'_1) - \frac{1}{2} \cdot 2\mu^2\phi'_1\phi'_1 \\ & - \frac{1}{4}(F^{\mu\nu}F_{\mu\nu}) + \frac{1}{2} \cdot e^2\phi_0^2A_\mu A^\nu \\ & + \phi_0e^2\phi'_1A_\mu A^\mu + \frac{1}{2}e^2\phi'^2A_\mu A^\mu + \mathcal{O}(\phi'^3)\dots\end{aligned}\quad (2.40)$$

247 The degree of freedom that ϕ_2 represents, is absorbed as a longitudinal polarization of the
248 A_{mu} field, a forbidden for massless gauge bosons, but necessary for massive bosons.

249 For this case of an abelian symmetry $U(1)$, it was shown that if a complex scalar field, which
250 interacts with itself and another vector field, can gain a non-zero vacuum expectation value.
251 The Lagrangian can be expanded about this new minimum, generating a mass term for the
252 vector field. One of the degrees of freedom of the original complex scalar field is then absorbed
253 as a longitudinal polarization state of the massive vector field.

254 2.5 The Higgs Mechanism in a non-Abelian Theory

255 Before describing the electroweak gauge theory of $SU(2) \otimes U(1)$, it will be helpful to see the effects
256 of the Higgs mechanism for the non-Abelian group, $SU(2)$ by itself. Consider an example
257 of an $SU(2)$ gauge field coupled to a scalar field that transforms like a real-valued vector under
258 $SU(2)$ transformations [4]. The field ϕ will have the form:

$$\phi = \begin{pmatrix} \phi_1 \\ \phi_2 \\ \phi_3 \end{pmatrix} \quad (2.41)$$

259 where the components, ϕ_i are real-valued fields. The $SU(2)$ transformation for this scalar field
260 will also look like:

$$\phi \rightarrow e^{i\alpha^i T^i} \phi \quad (2.42)$$

261 where the matrices, T^i are defined as:

$$iT^1 = \begin{pmatrix} 0 & 0 & 0 \\ 0 & 0 & 1 \\ 0 & -1 & 0 \end{pmatrix}, \quad T^2 = \begin{pmatrix} 0 & 0 & -1 \\ 0 & 0 & 0 \\ 1 & 0 & 0 \end{pmatrix}, \quad T^3 = \begin{pmatrix} 0 & 1 & 0 \\ -1 & 0 & 0 \\ 0 & 0 & 0 \end{pmatrix} \quad (2.43)$$

262 The Lagrangian for this field will feature a Higgs potential term along with the previously
263 mentioned $SU(2)$ gauge fields, A_μ^a coupled to the scalar field, ϕ , and is given by:

$$\mathcal{L} = -\frac{1}{4}F_{\mu\nu}^a F^{a\mu\nu} + |D_\mu\phi|^2 + \mu^2\phi^*\phi - \frac{\lambda}{4}(\phi^*\phi)^2 \quad (2.44)$$

264 where $F_{\mu\nu}^a$, the field strength tensor is defined as:

$$F_{\mu\nu}^a = (\partial_\mu A_\nu^a - \partial_\nu A_\mu^a) + g\epsilon^{abc} A_\mu^b A_\nu^c \quad (2.45)$$

265 and the covariant derivative is defined as:

$$D_\mu = (\partial_\mu + igA_\mu^a T^a)\phi \quad (2.46)$$

266 Similarly to the Abelian case, the Higgs potential will induce a spontaneous symmetry breaking,
267 and one of the components of the field ϕ will gain a vacuum expectation value. After this
268 breaking and expanding around the ground state potential, the field ϕ will have the form:

$$\phi = \frac{1}{\sqrt{2}} \begin{pmatrix} 0 \\ 0 \\ v+h \end{pmatrix} \quad (2.47)$$

269 There has been no loss in generality in assuming this form since, similarly to the abelian case,
270 we can use the gauge symmetry of $SU(2)$ to rotate the field into this configuration. Goldstone's
271 theorem tells us that we should expect two massive gague bosons corresponding to the T^1 , and
272 T^2 generators, while the T^3 generator will correspond to a massless gauge boson, since ϕ is still
273 invariant under T^3 transformations.

274 As in the Abelian case, the mass terms for the gauge bosons are generated from the covariant
275 derivative term, $|D_\mu\phi|^2$

$$\begin{aligned} D_\mu\phi &= \frac{1}{\sqrt{2}} \left(\partial_\mu + gA_\mu^1 \begin{pmatrix} 0 & 0 & 0 \\ 0 & 0 & 1 \\ 0 & -1 & 0 \end{pmatrix} + gA_\mu^2 \begin{pmatrix} 0 & 0 & -1 \\ 0 & 0 & 0 \\ 1 & 0 & 0 \end{pmatrix} + gA_\mu^3 \begin{pmatrix} 0 & 1 & 0 \\ -1 & 0 & 0 \\ 0 & 0 & 0 \end{pmatrix} \right) \begin{pmatrix} 0 \\ 0 \\ v+h \end{pmatrix} \\ &= \frac{1}{\sqrt{2}} \begin{pmatrix} 0 \\ 0 \\ \partial_\mu \end{pmatrix} + \frac{gA_\mu^1}{\sqrt{2}} \begin{pmatrix} 0 \\ v+h \\ 0 \end{pmatrix} - \frac{gA_\mu^2}{\sqrt{2}} \begin{pmatrix} v+h \\ 0 \\ 0 \end{pmatrix} \\ &= \frac{1}{\sqrt{2}} \begin{pmatrix} g(v+h)A_\mu^1 \\ g(v+h)A_\mu^2 \\ \partial_\mu h \end{pmatrix} \end{aligned} \quad (2.48)$$

276 Therefore

$$|D_\mu \phi|^2 = \frac{1}{2} \partial_\mu h \partial^\mu h + \frac{g^2 v^2}{2} ((A_\mu^1)^2 + (A_\mu^2)^2) + \frac{g^2}{2} (h^2 + 2hv) ((A_\mu^1)^2 + (A_\mu^2)^2) \quad (2.49)$$

This theory produces two massive bosons, A_μ^1 and A_μ^2 , both with mass, $m_A = gv$. These fields have h , and h^2 couplings to the Higgs boson. The third gauge field, A_μ^3 , remains massless and is not coupled to the Higgs field. This model is beginning to resemble a description of electroweak physics, however, a third massive boson is necessary, as is a new gauge symmetry in order to generate it. That is the subject of the next section.

2.6 Glashow Weinberg Salam Theory

Glashow, Weinberg, and Salam published their theory unifying electromagnetic and weak forces in the 1960s [15] [16] [17]. It begins with the requirement of a $SU(2)_L \otimes U(1)$ symmetry and incorporates the Higgs mechanism to give mass to the gauge bosons of the weak force. As described earlier, the $U(1)$ symmetry requires introducing a vector field, which will be labeled B_μ , and an interaction term, which is absorbed into the covariant derivative, D_μ . The transformation will also be parameterized with a with a quantum number, Y , known as hypercharge. The $SU(2)$ symmetry requires the introduction of three new vector fields, which will be labeled $W_\mu^i, i = 1, 2, 3$. The quantum number associated with this gauge group is known as isospin, and is determined by the T^3 operator, acting on an $SU(2)$ doublet on the third generator of the group. The $SU(2) \otimes U(1)$ transformation, $U(x)$, will then be given by:

$$U(x) = e^{i\alpha^a(x)\tau^a} e^{iY\alpha(x)} \quad (2.50)$$

where $\tau^a = \sigma^a/2$, the Pauli matrices, 2.18. These gauge fields will be coupled, via the covariant derivative, to a doublet of complex scalar fields ϕ , with hypercharge $Y = +1/2$. A Higgs potential will be added to generate the spontaneous symmetry breaking that will give mass to three of the gauge fields, and leave one massless. In order to preserve the $SU(2)_L \otimes U(1)$ symmetry, the new covariant derivative will take the form:

$$D_\mu = (\partial_\mu - igW_\mu^a \tau^a - \frac{i}{2}g'B_\mu) \quad (2.51)$$

The subscript L on $SU(2)_L$ refers to the experimental results that the weak force violates parity maximally, by only interacting with the left-handed chiral component of a field. Right versus left chirality is determined by whether the spin of a particle is aligned or anti-aligned with its direction of motion, and in general a particle is represented by a linear combination

of its right and left handed components. This idea was first proposed by Chen Ning Yang and Tsung-Dao Lee, in the 1950s. Their ideas were validated by the experimental discovery of parity violation in 1957, through the beta decays of Cobalt 60 atoms by C.S Wu. That same year, Yang and Lee were awarded the nobel prize for their insight [18]. In this model, then, the left-handed components of the particles participate in the weak interaction and are formed into doublets, while the right handed components are singlets, and will only interact with the electromagnetic field, B_μ . The quantum numbers of the doublet will be given by +1/2 for the upper component of the $SU(2)$ doublet, and -1/2 for the lower component. The fermion content of this theory is then given by:

$$\begin{pmatrix} \nu_L \\ e_L \end{pmatrix}, e_R \quad \begin{pmatrix} u_L \\ d_L \end{pmatrix}, u_R, d_R \quad (2.52)$$

where the right handed neutrino, ν_R has been omitted, since it has zero charge, and isospin, and therefore does not participate in any of the interactions of this theory. The complete Lagrangian is given by a sum of free particle terms for massless bosons, fermions, and Higgs scalar fields; the Higgs potential; and a Yukawa coupling term between the fermions and the Higgs, which generates their masses.

$$\mathcal{L}_{GWS} = \mathcal{L}_{BosonKE} + \mathcal{L}_{Higgs} + \mathcal{L}_{FermionKE} + \mathcal{L}_{Yukawa} \quad (2.53)$$

The Higgs potential will have the form:

$$\mathcal{L}_{Higgs} = (D_\mu \phi)^\dagger (D^\mu \phi) + \mu^2 \phi^\dagger \phi - \lambda (\phi^\dagger \phi)^2 \quad (2.54)$$

The Higgs potential will break the symmetry of the Lagrangian when one of the four degrees of freedom in the complex scalar doublet, ϕ , spontaneously acquires a vacuum expectation value. In this case, it will generate three massive gauge bosons, one massless gauge boson, and a massive scalar field. After gaining a vacuum expectation value, and expanding about this value, the scalar fields will have the form:

$$\langle \phi \rangle = \frac{1}{\sqrt{2}} \begin{pmatrix} 0 \\ v + h \end{pmatrix} \quad (2.55)$$

where no loss of generality has occurred since we are always able to rotate into this form through the appropriate gauge transformations, similar to what was described in the Abelian case. It should also be noted that this form is not invariant to any of the individual generators t^a , however ϕ will be invariant to a combination of $T^3 + Y$ generators. Per Goldstone's theorem, we

should expect this linear combination of fields to be the massless vector boson after symmetry breaking. The massless eigenstate will be the electromagnetic field, $A_\mu \sim A_\mu^3 + B_\mu$. The electric charge quantum number, Q , is then defined as

$$Q = T^3 + Y \quad (2.56)$$

³²¹ As before, the generation of the masses for the gauge bosons are generated by the interaction
³²² of their fields with the Higgs field via the covariant derivative.

$$\begin{aligned} D_\mu \phi &= \frac{1}{\sqrt{2}} \left(\partial_\mu - \frac{ig}{2} A_\mu^1 \begin{pmatrix} 0 & 1 \\ 1 & 0 \end{pmatrix} - \frac{ig}{2} A_\mu^2 \begin{pmatrix} 0 & -i \\ i & 0 \end{pmatrix} - \frac{ig}{2} A_\mu^3 \begin{pmatrix} 1 & 0 \\ 0 & -1 \end{pmatrix} \right) \begin{pmatrix} 0 \\ v+h \end{pmatrix} \\ &= \frac{1}{\sqrt{2}} \left(\partial_\mu + i(\frac{1}{2}(v+h)(gA_\mu^3 - g'B_\mu)) \right) \end{aligned} \quad (2.57)$$

³²³ Taking the dot product of this with its hermitian conjugate gives the $|D_\mu \phi|^2$ term:

$$\begin{aligned} |D_\mu \phi|^2 &= \frac{1}{2} \partial_\mu h \partial^\mu h + \frac{1}{2} \frac{g^2 v^2}{4} ((A_\mu^1)^2 + (A_\mu^2)^2) + \frac{v^2}{4} (gA_\mu^3 - g'B_\mu)^2 \\ &\quad + \frac{1}{2} g^2 4(h^2 + 2vh)((A_\mu^1)^2 + (A_\mu^2)^2) + \frac{1}{2} \frac{1}{4} (h^2 + 2vh)(gA_\mu^3 - g'B_\mu) \end{aligned} \quad (2.58)$$

³²⁴ From equation 2.58 we can identify three massive and one massless gauge bosons, corresponding
³²⁵ to the charged and neutral weak currents, and the electromagnetic current.

$$\begin{aligned} W_\mu^\pm &= \frac{1}{\sqrt{2}} (A_\mu^1 \mp iA_\mu^2) && \text{with mass } m_W = g \frac{v}{2}; \\ Z_\mu^0 &= \frac{1}{\sqrt{g^2 + g'^2}} (gW_\mu^3 - g'B_\mu) && \text{with mass } m_Z = \frac{v}{2} \sqrt{g^2 + g'^2}; \\ A_\mu &= \frac{1}{\sqrt{g^2 + g'^2}} (gW_\mu^3 + g'B_\mu) && \text{with mass } m_A = 0; \end{aligned} \quad (2.59)$$

³²⁶ where the last field, A_μ is absent from the covariant derivative term, but already identified as
³²⁷ the massless gauge boson of the theory due to its gauge invariance under a $T^3 + Y$ rotation.
³²⁸ Using these definitions the covariant derivative has the following form:

$$\begin{aligned} D_\mu &= \partial_\mu - \frac{ig}{\sqrt{2}} (W^+ T^+ + W^- T^-) \\ &\quad - \frac{i}{\sqrt{g^2 + g'^2}} Z_\mu^0 (gT^3 - g'Y) - \frac{gg'}{\sqrt{g^2 + g'^2}} A_\mu (T^3 + Y) \end{aligned} \quad (2.60)$$

³²⁹ where $T^\pm = \frac{1}{2}(\sigma^1 \pm \sigma^2)$. From this form, we can identify the fundamental electric charge, e , as

$$e = \frac{gg'}{\sqrt{g^2 + g'^2}} \quad (2.61)$$

³³⁰ The similarity in the forms between Z_μ^0 and A_μ suggest that their relationship can be ex-
³³¹ pressed in a simpler form, as the rotation of underlying guage fields A_μ^3 and B_μ through the
³³² weak mixing angle, θ_W

$$\begin{pmatrix} Z_\mu^0 \\ A_\mu \end{pmatrix} = \begin{pmatrix} \cos \theta_W & -\sin \theta_W \\ \sin \theta_W & \cos \theta_W \end{pmatrix} \begin{pmatrix} A_\mu^3 \\ B_\mu \end{pmatrix} \quad (2.62)$$

³³³ where $\tan \theta_W = \frac{g'}{g}$. Expanding 2.62, we have the definitions of the Z_μ^0 and A_μ fields in terms of
³³⁴ θ_W

$$\begin{aligned} Z_\mu^0 &= A_\mu^3 \cos \theta_W - B_\mu \sin \theta_W \\ A_\mu &= A_\mu^3 \sin \theta_W + B_\mu \cos \theta_W \end{aligned} \quad (2.63)$$

³³⁵ The weak mixing angle, θ_W , also provides a simple relationship between the W_μ^\pm and Z_μ^0 fields:

$$m_W = m_Z \cos \theta_W \quad (2.64)$$

³³⁶ The covariant derivative, D_μ is also rewritten in terms of the mass eingenstates of the gauge
³³⁷ fields

$$D_\mu = (\partial_\mu - \frac{ig}{\sqrt{2}}(W_\mu^+ + W_\mu^- T^-) - \frac{ig}{\cos \theta_W} Z_\mu^0(T_3 - \sin^2 \theta_W Q) - ieA_\mu Q) \quad (2.65)$$

³³⁸ where $g = e/\cos \theta_W$. The square of the covariant derivative is then written as

$$\begin{aligned} |D_\mu|^2 &= \frac{1}{2}\partial_\mu h \partial^\mu h + \frac{1}{2}m_W^2 W_\mu^+ W^{\mu+} + \frac{1}{2}m_W^2 W_\mu^- W^{\mu-} + \frac{1}{2}m_Z^2 Z_\mu^0 Z^{\mu 0} \\ &\quad + \left(\frac{h^2}{v^2} + \frac{h}{v}\right)\left[\frac{1}{2}m_W^2(W_\mu^+ W^{\mu+} + W_\mu^- W^{\mu-}) + \frac{1}{2}m_Z^2 Z_\mu^0 Z^{\mu 0}\right] \end{aligned} \quad (2.66)$$

³³⁹

³⁴⁰

³⁴¹ With the form of the covariant derivative in place, the fermionic kinematic term of the
³⁴² Lagrangian can be described. As mentioned earlier, the masses of the fermions in the model
³⁴³ will be generated by the Yukawa interaction term with the Higgs, so this term only involves the
³⁴⁴ covariant derivatives acting on the left-handed doublet and right-handed singlet states of this
³⁴⁵ model.

³⁴⁶ The quantum number assignments for the leptons, which are chosen in order to reproduce the
³⁴⁷ known values of their electric charges, are shown in table 2.1. The values of these quantum

	ν_L	e_L	e_R	u_L	d_L	u_R	d_R
Isospin	+1/2	-1/2	0	+1/2	-1/2	0	0
Hypercharge	-1/2	-1/2	-1	+1/6	1/3	2/3	-1/3
Electric Charge	0	-1	-1	2/3	-1/3	2/3	-1/3

Table 2.1: The quantum numbers Isospin and Hypercharge are assigned for each of the $SU(2)$ and $U(1)$ symmetries respectively

numbers enter into the covariant derivative via the Z_μ^0 term of equation 2.65. The fermionic kinetic energy term of the Lagrangian is given by:

$$\begin{aligned} \mathcal{L}_{Fermion} = & \bar{E}_L(i\gamma^\mu D_\mu)E_L + \bar{e}_R(i\gamma^\mu D_\mu)e_R \\ & \bar{Q}_L(i\gamma^\mu D_\mu)Q_L + \bar{u}_R(i\gamma^\mu D_\mu)u_R + \bar{d}_R(i\gamma^\mu D_\mu)d_R \end{aligned} \quad (2.67)$$

Expanding the covariant term for the left-handed electron shows its explicit coupling to the gauge boson fields.

$$\begin{aligned} \mathcal{L}_{E_L} = & \begin{pmatrix} \bar{\nu}_L & \bar{e}_L \end{pmatrix} \left((i\gamma^\mu(\partial_\mu - \frac{ig}{\sqrt{2}}(W_\mu^+T^+ + W_\mu^-T^-) - \frac{ig}{\cos\theta_W}Z_\mu^0(T^3 - \sin^2\theta_W Q) - ieA_\mu Q)) \right) \begin{pmatrix} \nu_L \\ e_L \end{pmatrix} \\ = & \bar{\nu}_L i\gamma^\mu \partial_\mu \nu_L + \bar{e}_L i\gamma^\mu \partial_\mu e_L + \frac{ig}{\sqrt{2}} W_\mu^+ \bar{\nu}_L \gamma^\mu e + \frac{ig}{\sqrt{2}} W_\mu^- \bar{e}_L \gamma^\mu \nu_L \\ & + \frac{ig}{\cos\theta_W} \bar{\nu}_L (1/2) \gamma^\mu \nu_L + \frac{ig}{\cos\theta_W} \bar{e}_L \gamma^\mu (-1/2 + \sin^2\theta_W (+1)) e_L + (ie) \bar{e}_L \gamma^\mu A_\mu (-1) \end{aligned} \quad (2.68)$$

All of the terms will be combined with the final, spontaneously broken GWS Lagranian at the end of this section.

The final term to discuss in the theory, before combing all of the results, is the Yukawa interaction term between the fermion fields and the Higgs. For the electron, this term takes the form:

$$\begin{aligned} \mathcal{L}_{Yukawa} = & -\lambda_e \bar{E}_L \cdot \phi e_R - \lambda_e E_L \cdot \phi \bar{e}_R \\ = & -\frac{\lambda_e}{\sqrt{2}} (v+h)(\bar{e}_L e_R + e_L \bar{e}_R) \\ = & -\frac{\lambda_e v}{\sqrt{2}} (\bar{e}_L e_R + e_L \bar{e}_R) - \frac{\lambda_e}{\sqrt{2}} (\bar{e}_L e_R + e_L \bar{e}_R) h \end{aligned} \quad (2.69)$$

where the mass of the electron is identified as $m_e = \frac{\lambda_e v}{\sqrt{2}}$. In order to generate the masses of the particles, each fermion has its own unique λ value. So while the Higgs mechanism is able to generate the masses in a way that preserves the underlying $SU(2) \otimes U(1)$ symmetry, it does not explain the heirarchy of masses since each λ value is unique to each lepton. The second term in last equation of 2.69 is the coupling of the Higgs particle, h , to the fermions. The coupling is proportional to the mass of the particle. The largest of these is to the top quark,

³⁶³ with $m_t = 73.21 \pm 0.51 \pm 0.71 \text{ GeV}$.

³⁶⁴ The Yukawa coupling for the quarks is necessarily modified when additional quarks besides
³⁶⁵ the u and d are added to the theory. This is because there can be additional coupling terms
³⁶⁶ that mix generations. This occurs when the mass eigenstate of the quarks is not the same as the
³⁶⁷ interaction eigenstate. The modification requires the expansion of the u_L and d_L components
³⁶⁸ into a vector of left handed quarks. If we let

$$u_L^i = (u_L, c_L, t_L), \quad d_L^i = (d_L, s_L, b_L) \quad (2.70)$$

³⁶⁹ represent the up and down-type quarks in the original weak interaction basis, then the vectors,
³⁷⁰ u_L^i and d_L^i , can be defined as the diagonalized basis for the Higgs coupling. They are related
³⁷¹ through a unitary transformation.

$$u_L^i = U_u^{ij} u_L^{j\prime}, \quad d_L^i = U_d^{ij} d_L^{j\prime} \quad (2.71)$$

³⁷² The interaction terms with the charged gauge boson currents must then be rewritten as

$$J_W^{\mu+} = \frac{1}{\sqrt{2}} \bar{u}_L^i \gamma^\mu d_L^i = \frac{1}{\sqrt{2}} \bar{u}_L^{i\prime} \gamma^\mu (U_u^\dagger U_d) d_L^{j\prime} = \frac{1}{\sqrt{2}} \bar{u}_L^{i\prime} \gamma^\mu V_{ij} d_L^{j\prime} \quad (2.72)$$

³⁷³ where V_{ij} is the 3x3 Cabibbo-Kobayashi-Maskawa (CKM) matrix describing the mixing among
³⁷⁴ six quarks [19] [20]. It is an extension of the Glashow-Iliopoulos-Maiani mechanism, which
³⁷⁵ was a 2x2 matrix that predicted the existence of a fourth quark, the charm quark. The GIM
³⁷⁶ mechanism was an attempt to suppress flavor-changing-neutral currents, which occur at LO in
³⁷⁷ a three-quark model, but not in a four-quark model. The CKM matrix, however, was motivated
³⁷⁸ by an attempt to explain CP violation in the weak interaction. At the time of its publication,
³⁷⁹ the bottom and top quarks were not predicted. After these were discovered, they were awarded
³⁸⁰ the nobel prize in physics in 2008.

³⁸¹ At this point, all the pieces are ready to write down the GWS Lagrangian, after the
³⁸² Higgs mechanism has spontaneously broken the $SU(2) \otimes U(1)$ symmetry.

$$\begin{aligned} \mathcal{L}_{Unbroken} = & -\frac{1}{4} A_{\mu\nu}^a A^{\mu\nu a} - \frac{1}{4} F_{\mu\nu} F^{\mu\nu} \\ & + |D_\mu \phi|^2 + \mu^2 (\phi^\dagger \phi) - \lambda (\phi^\dagger \phi)^2 \\ & + \bar{E}_L (i\gamma^\mu D_\mu) E_L + \text{similar terms for } e_R, U_L, u_R, d_R \\ & - \lambda_e \bar{E}_L \cdot \phi e_R + h.c. + \text{similar terms for } e_R, U_L, u_R, d_R \end{aligned} \quad (2.73)$$

$$\begin{aligned}
\mathcal{L}_{GWS} = & -\frac{1}{4}(Z_{\mu\nu}^0)^2 - \frac{1}{2}(W_{\mu\nu}^+ W_{\mu\nu}^-) - \frac{1}{4}(F_{\mu\nu})^2 \\
& + ig \cos \theta_W ((W_\mu^- W_\nu^+ - W_\nu^- W_\mu^+) \partial^\mu Z^{0\nu} + W_{\mu\nu}^+ W^{-\mu} Z^{0\nu} + W_{\mu\nu}^- W^{+\mu} Z^{0\nu}) \\
& + ie ((W_\mu^- W_\nu^+ - W_\nu^- W_\mu^+) \partial^\mu A^\nu + W_{\mu\nu}^+ W^{-\mu} A^\nu - W_{\mu\nu}^- W^{+\mu} A^\nu) \\
& + g^2 \cos^2 \theta_W (W_\mu^+ W_\nu^- Z^{0\mu} Z^{0\nu} - W_\mu^+ W^{-\mu} Z_\nu^0 Z^{0\nu}) \\
& + g^2 (W_\mu^+ W_\mu^- A^\mu A^\nu - W_\mu^+ W^{-\mu} A_\nu A^\nu) \\
& + ge \cos \theta_W (W_\mu^+ W_\nu^- (Z^{0\mu} A_\nu + Z^{0\nu} A^\mu) - 2W_\mu^+ W^{-\mu} A^\nu) \\
& + \frac{1}{2}g^2 (W_\mu^+ W_\nu^-) (W^{+\mu} W^{-\nu} - W^{+\nu} W^{-\mu}) \\
& + \frac{1}{2}\partial_\mu h \partial^\nu h - v^2 \lambda h^2 + \frac{1}{2}m_W^2 W_\mu^+ W^{+\mu} + \frac{1}{2}m_W^2 W_\mu^- W^{-\mu} + \frac{1}{2}m_Z^2 Z_\mu^0 Z^{0\mu} \\
& + \left(\frac{h^2}{v^2} + \frac{h}{v}\right) \left(\frac{1}{2}m_W^2 (W_\mu^+ W^{+\mu} + W_\mu^- W^{-\mu}) + \frac{1}{2}m_Z^2 Z_\mu^0 Z^{0\mu}\right) - \lambda v h^3 - \frac{1}{4}\lambda h^4 \\
& + \bar{E}_L (i\gamma^\mu \partial_\mu) E_L + e_R^- (i\gamma^\mu \partial_\mu) e_R + \bar{Q}_L (i\gamma^\mu \partial_\mu) Q_L + u_R^- (i\gamma^\mu \partial_\mu) u_R + \bar{d}_R (i\gamma^\mu \partial_\mu) d_R \\
& + g (W_\mu^+ J_W^{\mu+} + W_\mu^- J_W^{\mu-} + Z_\mu^0 J_Z^\mu) + e A_\mu J_{EM}^\mu \\
& - \frac{\lambda_e v}{\sqrt{2}} (\bar{e}_L e_R + \bar{e}_R e_L) - \frac{\lambda_e h}{\sqrt{2}} (\bar{e}_L e_R + \bar{e}_R e_L) \\
& - \frac{\lambda_u v}{\sqrt{2}} (\bar{u}_L u_R + \bar{u}_R u_L) - \frac{\lambda_u h}{\sqrt{2}} (\bar{u}_L u_R + \bar{u}_R u_L) \\
& - \frac{\lambda_d v}{\sqrt{2}} (\bar{d}_L d_R + \bar{d}_R d_L) - \frac{\lambda_d h}{\sqrt{2}} (\bar{d}_L d_R + \bar{d}_R d_L)
\end{aligned} \tag{2.74}$$

where the currents of the electroweak interaction, $J_W^{\mu+}$, $J_W^{\mu-}$, J_Z^μ , J_A^μ are defined as:

$$\begin{aligned}
J_W^{\mu+} &= \frac{1}{\sqrt{2}} (\bar{\nu}_L \gamma^\mu e_L + \bar{u}_L^i \gamma^\mu V_{ij} d_L^j) \\
J_W^{\mu-} &= \frac{1}{\sqrt{2}} (\bar{e}_L \gamma^\mu \nu_L + \bar{d}_L^i \gamma^\mu V_{ij} u_L^j) \\
J_Z^\mu &= \frac{1}{\cos \theta_W} (\bar{\nu}_L \gamma^\mu (+1/2) \nu_L + \bar{e}_L \gamma^\mu (-1/2 + \sin^2 \theta_W) e_L + \bar{e}_R \gamma^\mu \sin^2 \theta_W e_R \\
&\quad + \bar{u}_L \gamma^\mu (1/2 - 2/3 \sin^2 \theta_W) u_L + \bar{u}_R \gamma^\mu (-2/3 \sin^2 \theta_W) u_R \\
&\quad + \bar{d}_L \gamma^{mu} (-1/2 + 1/3 \sin^2 \theta_W) d_L + \bar{d}_R \gamma^\mu (1/3 \sin^2 \theta_W) d_R) \\
J_{EM}^\mu &= e_{L,R}^- \gamma^\mu (-1) e_{L,R} + u_{L,R}^- \gamma^\mu (2/3) u_{L,R} + d_{L,R}^- \gamma^\mu (-2/3) d_{L,R}
\end{aligned} \tag{2.75}$$

383 2.7 The Standard Model of Particle Physics

The Standard Model of particle physics, extends the GWS model by incorporating the QCD interaction between the quarks and gluons. The symmetry of this theory is that of:

$$SU(3)_C \otimes SU(2)_L \otimes U(1)_Y \tag{2.76}$$

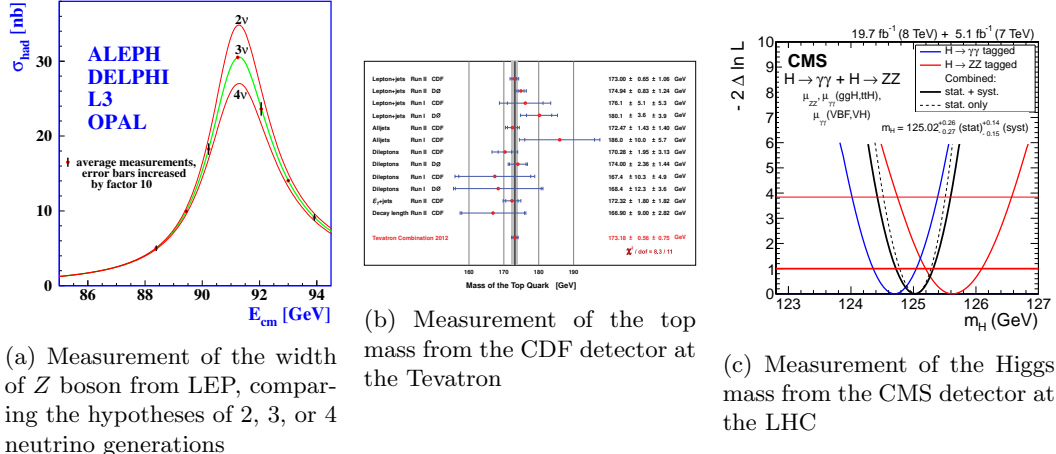


Figure 2.4: Experimental milestones of the Standard Model

³⁸⁴ The Lagrangian of the model is given by

$$\mathcal{L}_{SM} = \mathcal{L}_{GWS} - \frac{1}{4} G_{\mu\nu}^a G^{a\mu\nu} + g_S C_\mu^a J_{QCD}^{a\mu} \quad (2.77)$$

³⁸⁵ where the current for the QCD interaction, $J_{QCD}^{a\mu}$ is defined as:

$$J_{QCD}^a = \bar{u}^i \gamma^\mu t^a u^i + \bar{d}^i \gamma^\mu t^a d^i \quad (2.78)$$

³⁸⁶ where t^a are the Gell-Mann matrices defined in equation 2.30. The field strength tensor for the
³⁸⁷ eight gluon fields, $G_{\mu\nu}^a$, is defined as

$$G_{\mu\nu}^a = (\partial_\mu C_\nu^a - \partial_\nu C_\mu^a) - g_S f^{abc} C_\mu^b C_\nu^c \quad (2.79)$$

³⁸⁸ The experimental evidence in favor of the SM is compelling. It has not only been able
³⁸⁹ to describe existing phenomenon to great precision, but has also predicted the existence of
³⁹⁰ new forms of matter and interactions among fundamental particles. The UA1 [21] [22] and
³⁹¹ UA2 [23] [24] experiments at CERN, under the leadership of Carlo Rubbia, discovered the
³⁹² W and Z bosons in 1983. The experiments observed a handful of events, in $p\bar{b}$ collisions, at
³⁹³ $\sqrt{s} = 540$ GeV, and were able to measure the masses to be $M_W \sim 80$ GeV and $M_Z \sim 95$ GeV.

³⁹⁴ In the following years, from 1989-2000, the Large electron-positron (LEP) collider at CERN
³⁹⁵ conducted precision measurements of the Standard Model [25] [26]. Along with high-precision
³⁹⁶ measurements on the W, Z masses:

$$m_Z = 91.1875 \pm 0.0021 \text{ GeV} \quad (2.80)$$

$$m_W = 80.376 \pm 0.0033 \text{ GeV}$$

³⁹⁷ the experiment was also able to put stringent limits on the existence of more than three families of

398 leptons and quarks by measuring the width of the Z boson. Figure 2.4(a) shows the comparison
399 of two, three, and four family hypotheses to data.

400 Another milestone for the Standard Model occurred in 1995 when the CDF [27] and D0 experiments
401 [28] at the Tevatron announced the observation of the top quark, with $m_t \sim 176$ GeV,
402 in $p\bar{p}$ collisions at $\sqrt{s} = 1.8$ TeV. Figure 2.4(c) shows a plot from 2012, the latest top quark
403 mass measurements from CDF, which reports a $m_t = 173.18 \pm 0.56 \pm 0.75$ GeV. It was the
404 last quark predicted by the CKM matrix to be observed, and earned Makoto Kobayashi and
405 Toshihide Maskawa the nobel prize in 2008 for their work extending the quark sector to three
406 families and parameterizing their electroweak mixing.

407 Yet another milestone was reached in 2012, when the CMS and ATLAS detectors at CERN
408 announced the observation of a new boson, with characteristics strikingly similar to the elusive
409 Higgs boson of the SM. Figure 2.4(c) shows the latest measurement results on the mass from the
410 $H \rightarrow \gamma\gamma$ and $H \rightarrow ZZ$ channels, with a $m_H = 125.02 \pm 0.27 \pm 0.15$. One of the most important
411 remaining goals is to measure the couplings of this new boson to all of the other particles in
412 the Standard Model. Of particular interest is the coupling to the top-quark, since it offers the
413 largest value of the Higgs Yukawa coupling to measure. This offers a test of the nature of the
414 coupling, as well as a probe into deviations from its value.

415 2.8 Higgs Production in pp Collisions at the LHC

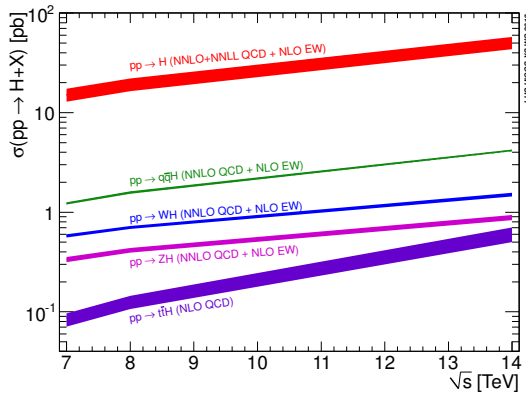


Figure 2.5: Higgs production cross-sections at the LHC, for 7–14 TeV pp collisions

416 The rest of the thesis will describe the search for Higgs boson production in proton-proton
417 collisions at the LHC, so it will be useful to understand the production mechanisms for the Higgs
418 in this scenario. At the LHC collision energies 7 – 14 TeV, there are four dominant production
419 mechanisms that produce Higgs events: gluon-gluon fusion (ggf), vector-boson fusion (vbf),
420 associated production with vector bosons (VH), and associated production with top-quark pairs
421 (tth). Figure 2.5 shows the relative cross sections for each of these mechanisms.

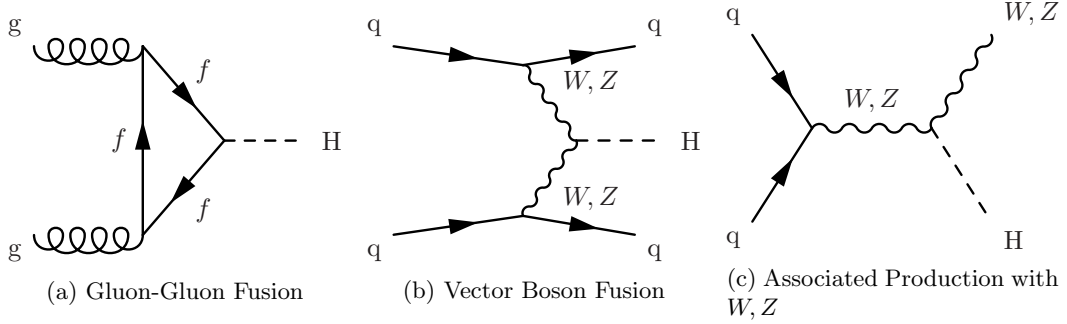


Figure 2.6: Feynman diagrams for the three largest Higgs production modes at the LHC

Gluon-gluon fusion, which proceeds via a heavy quark loop [29], is the dominant production mechanism at the LHC. The QCD radiative corrections to the total cross section have been computed at the next-to-leading order (NLO) and at the next-to-next-to-leading order (NNLO accuracy). The cross section for Higgs production at $m_H = 125$ GeV and $\sqrt{s} = 8$ TeV, the cross section is given as:

$$\sigma_{ggF} = 19.27 \pm \text{QCD Scale Unc.}^{+7.2\%}_{-7.8\%} \pm \text{PDF} + \alpha_S \text{ Unc.}^{+7.4\%}_{-6.9\%} \text{ pb}^{-1} \quad (2.81)$$

⁴²² Figure 2.6(a) shows a Feynman diagram for this process. The triangle loop contains all strongly
⁴²³ coupled fermions, which is dominated by the top-quark since the Yukawa coupling to the Higgs
⁴²⁴ is the largest.

Vector boson fusion proceeds through the fusion of W^+W^- or Z^0Z^0 gauge bosons [29]. The characteristic signature of the production mode is the associated production of two quarks, typically at a low angle relative to the proton beam. This process has been calculated to NNLO for QCD and NLO for Electroweak corrections [29]. The cross section at $m_H = 125$ GeV and $\sqrt{s} = 8$ TeV is given as:

$$\sigma_{VBF} = 1.653 \pm \text{EW Unc.}^{+4.5\%}_{-4.5\%} \pm \text{QCD Scale Unc.}^{+0.2\%}_{-0.2\%} \pm \text{PDF} + \alpha_S \text{ Unc.}^{+2.6\%}_{-2.8\%} \text{ pb}^{-1} \quad (2.82)$$

⁴²⁵ Figure 2.6(b) shows a Feynman diagram for VBF production. The large coupling to the W, Z
⁴²⁶ bosons helps to make this the sub-dominant production mechanism at the LHC. However, the
⁴²⁷ gluon content of the proton at TeV energies is much larger than that of the valence quarks, thus
⁴²⁸ the relative suppression.

The third largest production mechanism for Higgs bosons at the LHC is through associated production with a W or Z boson [29]. It has been calculated to NNLO for QCD and NLO for Electroweak corrections. This process is also sometimes referred to as, Higgstrahlung, since it resembles the bremsstrahlung process of an electron radiating a photon. The higher order

electroweak corrections are similar to that of the Drell-Yan, so much of the technology to compute the cross-section can be borrowed from existing EW calculations. The cross section for $m_H = 125 \text{ GeV}$ and $\sqrt{s} = 8 \text{ TeV}$ is:

$$\begin{aligned}\sigma_{WH} &= 0.7046 \pm \text{QCD Scale Unc.}^{+1.0\%}_{-1.0\%} \pm \text{PDF}+\alpha_S \text{ Unc.}^{+2.3\%}_{-2.3\%} \text{ pb}^{-1} \\ \sigma_{ZH} &= 0.4153 \pm \text{QCD Scale Unc.}^{+3.1\%}_{-3.1\%} \pm \text{PDF}+\alpha_S \text{ Unc.}^{+2.5\%}_{-2.5\%} \text{ pb}^{-1}\end{aligned}\quad (2.83)$$

⁴²⁹ Figure 2.6(c) shows the Feynman diagram for VH production. This channel is most useful for
⁴³⁰ identifying hadronic decays of the Higgs, since the associated gauge boson can decay to leptons,
⁴³¹ giving a strong kinematic handle over backgrounds that would normally overwhelm a similar
⁴³² search in the ggF channel.

⁴³³ 2.9 $t\bar{t}H$ Production in pp Collisions at the LHC

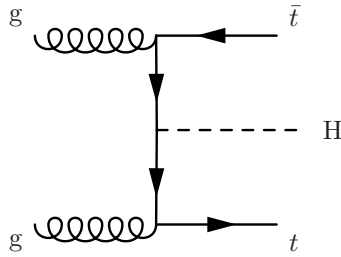


Figure 2.7: Feynman diagram for $t\bar{t}H$ production

⁴³⁴ The $t\bar{t}H$ production mode is the fourth largest production mode at the LHC [29]. This produc-
⁴³⁵ tion mode has been calculated to NLO in QCD [30] [31] and has been studied recently with the
⁴³⁶ state of the art NLO tools using the aMC@NLO [32] and POWHEG (PYTHIA+HERWIG) [33]
⁴³⁷ frameworks. Studies have also been performed interfacing NLO QCD studies [34] with the
⁴³⁸ Sherpa parton shower framework [35]. Additional studies on the effects of spin correlations with
⁴³⁹ the aMC@NLO and Madspin framework have also been performed [36].

It has been found that the addition of NLO effects increases the cross-section relative to LO by $\sim 20\%$. The largest theoretical uncertainty comes from the variation of the renormalization and factorization scale, the QCD coupling α_S , and the PDF uncertainty. The renormalization and factorization scales are set to $\mu_R = \mu_F = (1/2)(m_T + m_T + m_H)$ and are varied by a factor of 2 to determine the cross-section's dependence on these parameters. Three different PDF sets, MSTW2008, CTEQ6.6, and NNPDF2.0 were used with the appropriate corresponding values of α_S to determine the combined effect of varying PDF+ α_S . The cross section for $m_H = 125 \text{ GeV}$

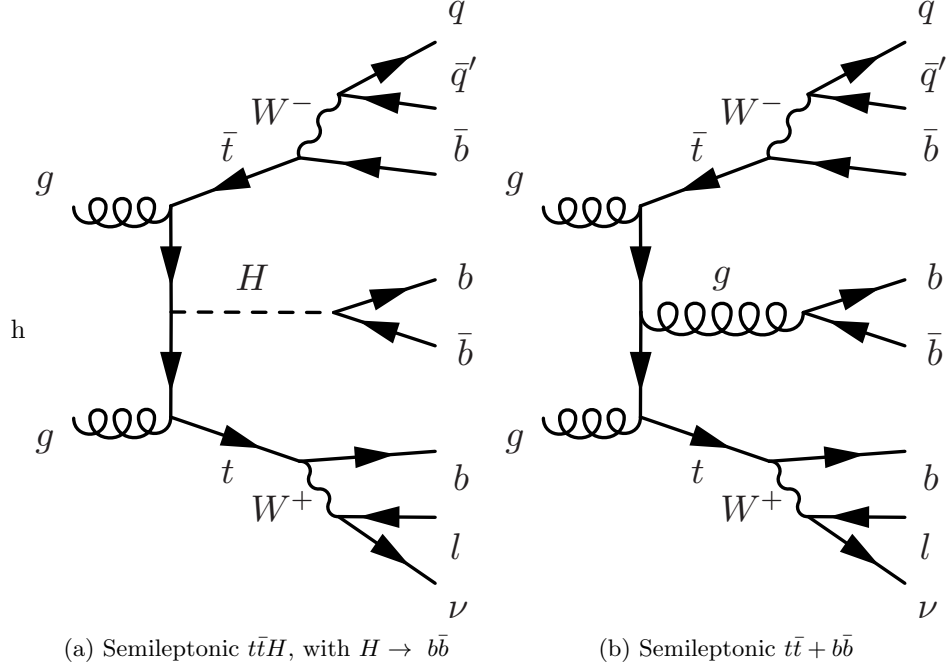


Figure 2.8: Feynman diagrams for the semileptonic $t\bar{t}H$ process and its irreducible background, $t\bar{t} + b\bar{b}$

and $\sqrt{s} = 8$ TeV is given by:

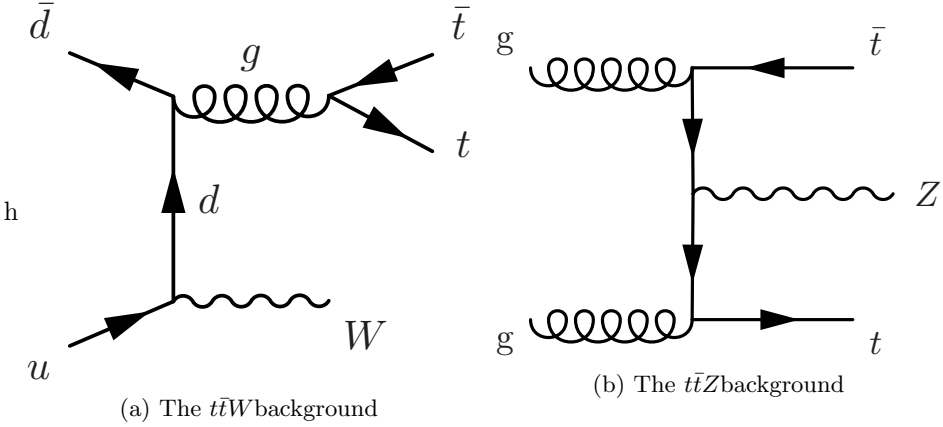
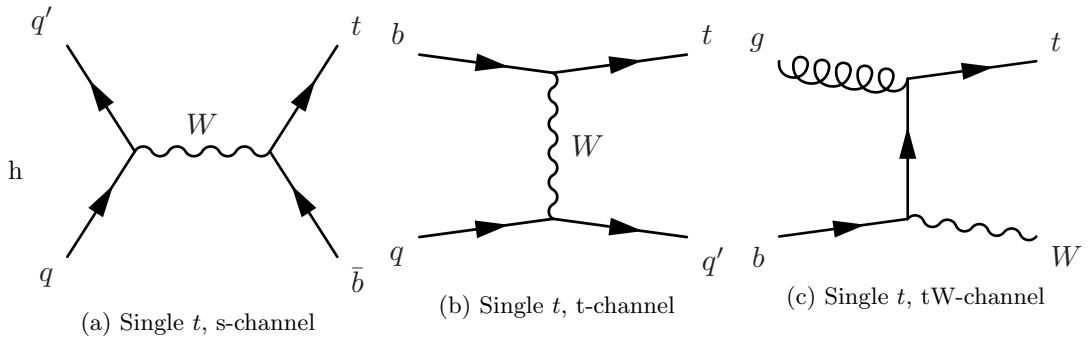
$$\sigma_{ttH} = 0.1293 \pm \text{QCD Scale Unc.}^{+3.8\%}_{-9.3\%} \pm \text{PDF} + \alpha_S \text{ Unc.}^{+8.1\%}_{-8.1\%} \text{ pb}^{-1} \quad (2.84)$$

440 A search for the Higgs in this production mode is additionally challenging due to this large
441 $\sim 10\%$ error on the theoretical cross-section. Figure 2.7 shows a Feynman diagram for this
442 process before the branching of the top-quarks or Higgs to final states.

443 When asking for the Higgs to decay to b-quark pairs, yet another complication arises when
444 trying to identify which b-quarks came from a top decay or from a Higgs decay. For example, in
445 the semileptonic decay of top quarks, there will be four b-quarks, and two light-flavor quarks in
446 the final state. This means there are 15 (six choose four) possibilities to associate quarks to the
447 top system. Although this is potentially constrained by b-tagging, and kinematic requirements
448 (such as forming the top or W masses), the number of remaining possibilites smears out the
449 resolution on peaking variables such as the invariant mass of b-quark pairs.

450 2.10 Background Processes to $t\bar{t}H$

451 The dominant background for $t\bar{t}H$ production of top-quark pairs with additional ISR/FSR jets,
452 $t\bar{t} + jets$. The irreducible component of this background is comes when the extra radiation
453 produces a final state with two additional b-quarks, $t\bar{t} + b\bar{b}$. Figure 2.8 compares the Feynman

Figure 2.9: Feynman diagrams for the $t\bar{t}W$ and $t\bar{t}Z$ background processesFigure 2.10: Feynman diagrams for the single t s,t, and tW background processes

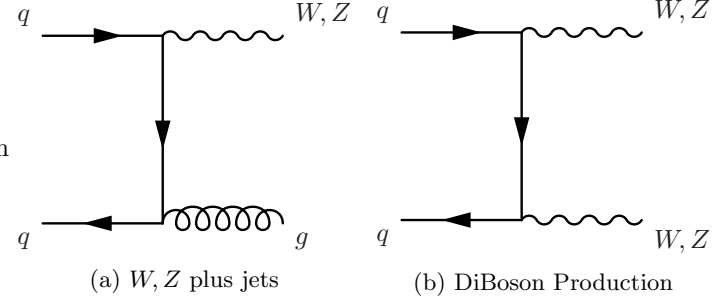
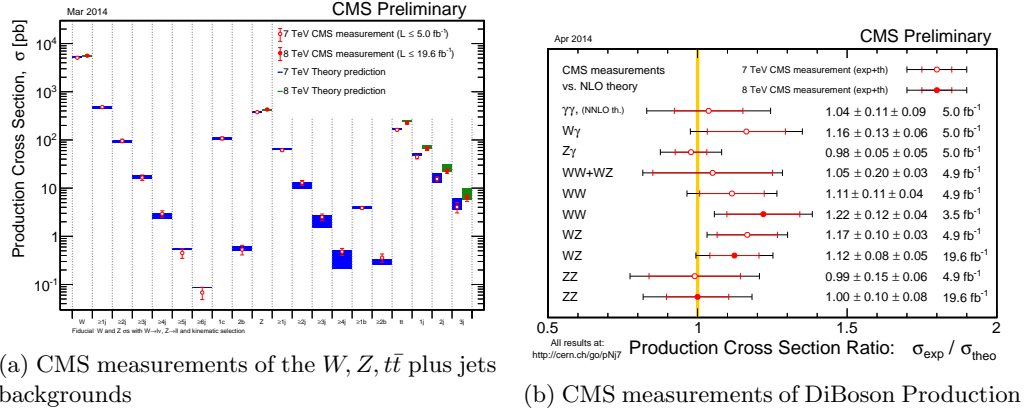
454 diagrams for the semileptonic decays of $t\bar{t}H$ and $t\bar{t} + b\bar{b}$.

455 Additional difficulties come from the theoretical uncertainty on the $t\bar{t} + b\bar{b}$ background [29].

456 The process has been calculated to NLO QCD in Sherpa [35] and OpenLoops [37] [38] [39]. It
457 has been found that depending on selection cuts, and use of NLO PDF inputs, the difference
458 between LO and NLO calculations on the cross section can be anywhere from 0.99% to 1.96%.

459 The light flavor component of the $t\bar{t} + jets$ background also enters in the selection when any
460 of the jets from the $t\bar{t}$ system or extra radiation are misidentified as b -jets. The cross-section
461 for the $t\bar{t} + jets$ process is $\sim 245 \text{ pb}^{-1}$. This is a factor of 1800, so even if a b -tagging algorithm
462 performs with a 1% mis-identification rate of light-jets, there will still be a large contribution
463 from this process that will leave a very similar signature in the detector as $t\bar{t}H$.

464 The next largest background is the production of vector bosons in association with top-
465 quark pairs, $t\bar{t}W$ and $t\bar{t}Z$. Figure 2.9 shows Feynman diagrams from these two processes. They
466 have cross-sections of $\sigma_{ttW} = 0.249 \text{ pb}^{-1}$ and $\sigma_{ttZ} = 0.208 \text{ pb}^{-1}$, which are only a factor of
467 ~ 2 greater than the $t\bar{t}H$ process. These processes can enter the semileptonic $t\bar{t}H$ selection by a
468 semileptonic $t\bar{t}$ decay, while the vector bosons decay to quarks, or through a hadronic $t\bar{t}$ decay,
469 while the vector bosons decay to quarks, and in the case of $t\bar{t}Z$, if the leptons is not identified
470 in the reconstruction.

Figure 2.11: Feynman diagrams for the W, Z plus jets, and diBoson (WW, WZ, ZZ) production.Figure 2.12: Measurements of $t\bar{t}H$ backgrounds at CMS

Single top production is also an important background to consider in a search for $t\bar{t}H$ production.

Figure 2.10 shows Feynman diagrams for this process. It does not have as large of a contribution as the other backgrounds, since it requires additional radiation in order to have a similar final state jet multiplicity as $t\bar{t}H$. However, since a top-quark is still involved in the process, the final state kinematics of its decay products will be very similar. Single t production has a cross section of $\sigma_t = 71.3 \text{ pb}^{-1}$, while Single \bar{t} production has a cross section of $\sigma_{\bar{t}} = 43.6 \text{ pb}^{-1}$, due to charge asymmetry of the valence quarks of the proton

The last backgrounds to consider are the electroweak production of W and Z bosons in association with jets, as well as WW , WZ , and ZZ pairs in association with jets. Figure ?? shows the Feynman diagrams for these processes, where the V , stands in for either W or Z bosons. For a semileptonic selection of $t\bar{t}H$ events, Z plus jets events enter from a misidentification of one of the leptons from the Z boson decay. Extra FSR/ISR radiation is also to leave a similar signature in the signal region of a $t\bar{t}H$ search, so it mainly contributes to control regions of the data.

All of these backgrounds have been measured at CMS. With the exception of a small degree of tension in the WW cross-section measurement, all backgrounds are in good agreement with Standard Model predictions. Figure 2.12(a) shows the results of CMS measurements on $V+jets$ and $t\bar{t} + jets$ backgrounds. Figure 2.12(b) shows the same, but for diBoson production.

489 2.11 Potential BSM Effects on $t\bar{t}H$ production

490 The phenomenological motivation for the existence of physics beyond the Standard Model come
 491 from the observation of phenomenon or states of matter not described by the theory. Observations
 492 of the cosmic microwave background from the Plank telescope have estimated that only
 493 $\sim 5\%$ of the observable universe is composed of ordinary matter [40]. The remaining composition
 494 is divided between Dark Matter ($\sim 27\%$, and $\sim 68\%$ respectively). Evidence for Dark Matter
 495 also comes from discrepancies between the observed rotational velocities of galaxies, and the
 496 observed mass distributions, suggesting the presence of additional form of matter which does
 497 not interact electromagnetically [41].

498 Additionally, in 1998, the Super-Kamiokande experiment proved that neutrinos oscillated
 499 between flavors, implying indirectly that they also have mass [42]. This is something not de-
 500 scribed in the Standard Model of physics. Due to their neutral charge, these particles are
 501 extremely difficult to detect, so experiments have only been able to measure differences in the
 502 mass squared between the three mass eigenstates. In 2005, the KamLAND experiment reported
 503 $|\Delta m_{12}^2 = 0.000079 eV^2|$ [43]. In 2006, the MINOS experiment reported $|\Delta m_{23} = 0.0027 eV^2|$ [44].

504 One of the largest theoretical problems with the Standard Model, comes the mechanism which
 505 made it all possible- the Higgs. In equation 2.73 there are terms that couple the Higgs boson
 506 to itself, $-\lambda vh^3$, and $-\frac{1}{4}\lambda h^4$. When computing NLO effects, these terms lead to a divergence
 507 in the Higgs mass, when considering the effect of a loop of fermions on the Higgs propagator.
 508 The corrections are of the form $\Delta m_H = -\frac{\lambda_f^2}{8\pi^2} \Lambda_{UV}$. Where Λ_{UV} is the high energy cut off for the
 509 theory, which in the limit of a perfect theory, should extend to infinity. This is known as the
 510 hierarchy problem.

511 Beyond the Standard Model physics is a term that describes extensions of the Standard
 512 Model in order to describe the observed phenomenon. For the neutrino oscillations, a solution
 513 similar to CKM matrix has been proposed, the PontecorvoMakiNakagawaSakata (PMNS) ma-
 514 trix. This proposes that the mass eigenstates of the neutrino are linear combinations of the weak
 515 eigenstates, allowing for the mixing of flavors. Current experiments now seek to measure the
 516 free parameters of this matrix.

517 Both the dark matter and hierarchy problems suffer in the fact that there is no clear model,
 518 such as the PMNS matrix, to provide a theoretical solution. Out of the plethora of theories that
 519 attempt to solve these problems, supersymmetry (SUSY) is the most popular in the theoretical
 520 and experimental community. It suggests that there is a broken symmetry between fermions
 521 and bosons, and introduces a partner to each Standard Model particle with a spin quantum
 522 number less 1/2 [45]. For the hierarchy problem, this provides a set of particles to cancel out the

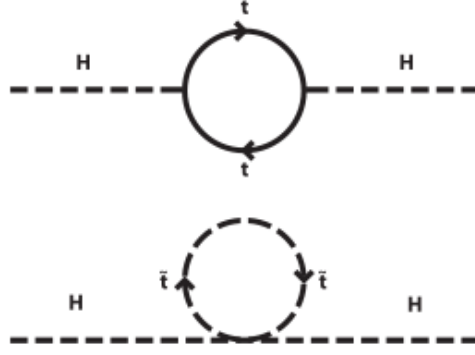


Figure 2.13: The cancellation of the divergent Higgs mass from a loop of top-quarks is cancelled by a loop of supersymmetric top-quarks, stop-quarks,

523 divergences in the NLO corrections to the Higgs mass. Figure 2.13 shows the Feynmann diagrams
 524 for a supersymmetric top-quark, or stop quark, that would cancel the divergent contribution from
 525 the Standard Model top quark. Depending on the specific form of the SUSY model, the stop
 526 quarks can potentially couple directly or indirectly to the top-quark, producing them at a higer
 527 rate during pp collisions. This would effect the number of observed events making it into the
 528 $t\bar{t}H$ selection.

529 A number of extensions to the SM also involve introducing new top-like particles into the
 530 theory. Vector-like quarks would be spin 1/2 particles that transform as triplets under the $SU(3)$
 531 color group and whose left and right-handed components have the same color and electroweak
 532 quantum numbers [46]. These objects are common to several different types of models. Little
 533 Higgs models [47] [48] [49], models with extra dimensions [50] [51], top-color models [52], and
 534 composite Higgs models [53], include a vector-like top partner, t' that decays to a top-quark and
 535 either a Higgs, W , or Z particle. Both $t't'$ pair production and $t't$ production would yield the $t\bar{t}H$
 536 final state, or at least one indistinguishable detector signature. $t\bar{t}H$ search can provide indirect
 537 limits on these models, by observing an excess or lack thereof of $t\bar{t}H$ events, without having to
 538 directly construct a t' resonance.

539 **Chapter 3**

540 **The Large Hadron Collider**



Figure 3.1: Aerial view of the LHC complex, spanning the French-Swiss border [1]

541 The Large Hadron Collider (LHC), is a superconducting, proton-proton, accelerator and
542 collider operated by the European Center for Nuclear Research (CERN) laboratory in Geneva,
543 Switzerland [54]. Figure 3.1 shows an aerial view of the LHC complex, with the main laboratory
544 campus being labeled as CERN, with four of the detector experiments being labeled as ALICE,
545 ATLAS, CMS, and LHCb. Three smaller experiments, not pictured, also use the LHC ring, and
546 are TOTEM, LHCf, and MOeDAL. It was designed to elucidate the mechanism of electroweak
547 symmetry breaking and explore TeV scale of particle physics. As such, it is required to produce
548 a large number of high center-of-mass energy events. The high center-of-mass energy allows the
549 creation of heavy particles, while a large luminosity allows for the creation of rare processes.
550 The number of events produced at a collider is a product of the luminosity of the collider and

551 the total cross-section for the objects being collided.

$$N_{events} = L\sigma_{event} \quad (3.1)$$

552 The cross-section, σ_{event} , can be estimated from the theory of the Standard Model as described
 553 in section 2.1 and validated by measurement at detectors, such as CMS, as shown in section 2.10.
 554 The luminosity is a control of the experiment, and for Gaussian distributed beams, is given by
 555 the equation:

$$L = \frac{N_b^2 n_b f_{rev} \gamma_r}{4\pi \epsilon_n \beta^*} F \quad (3.2)$$

556 The parameters of this equation and their value for the LHC is as follows:

- 557 • N_b - Number of particles per bunch, squared since there are two beams. The mechanism
 558 of achieving such high energies is based in Radio-Frequency (RF) cavity technology, which
 559 clusters the protons together into packets, which are all accelerated and collided together.
 560 For the LHC, $N_b = 1.15 \times 10^{11}$.
 - 561 • n_b - Number of bunches per beam. The maximum design for the LHC allows for $n_b = 2808$
 562 bunches, however in practice, lower number of bunches have been run with in order to
 563 create more time between bunch crossings.
 - 564 • f_{rev} - Revolution frequency of the protons in the LHC ring. This is determined by ring
 565 circumference, and for the LHC, $f_{rev} = 11.2$ kHz.
 - 566 • γ_r - This is the relativistic gamma-factor, determined by the speed, and thus the center of
 567 mass energy of the collisions.
 - 568 • ϵ_n - This is the normalized transverse emittance of the beam, which describes the RMS
 569 spread of the beam in its transverse plane. For the LHC $\epsilon_n = 3.75 \mu\text{m}$.
 - 570 • β^* - Is the minimum of the β function, which is defined as the square of the transverse
 571 beamsize divided by ϵ_n . It is minimized at interaction regions, where the beams are being
 572 squeezed into the smallest region possible, to maximize the probability of protons colliding
 573 during each bunch crossing. For the LHC, $\beta^* = 0.55$
 - 574 • F - This is the efficiency for having the two beams head-on, and is determined by the
 575 crossing angle at which the two counter-rotating beams meet each other.
- 576 The LHC is designed to deliver a maximum luminosity of $L = 10^{34} \text{ cm}^{-2}\text{s}^{-1}$ to the CMS and ATLAS
 577 experiments, with a maximum center-of-mass energy of $\sqrt{s} = 14$ TeV.

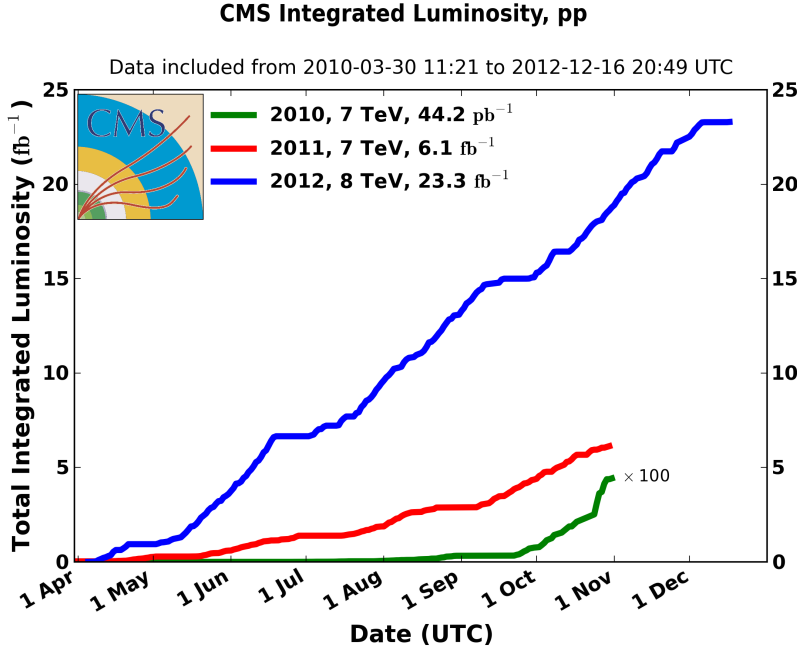


Figure 3.2: Integrated Luminosity delivered to the CMS experiment from 2010-12

578 In 2010-11, the LHC ran at center-of-mass energy, $\sqrt{s} = 7 \text{ TeV}$ and delivered $\sim 6 \text{ fb}^{-1}$ of
 579 data to the CMS experiment. In 2012, it ran at $\sqrt{s} = 8 \text{ TeV}$ and collected $\sim 23 \text{ fb}^{-1}$. Figure 3.2
 580 shows a diagram of the luminosity collected as a function of time for each year running.

581 The next sections will describe the LHC accelerator complex, the chain of events leading
 582 up to collisions of protons at the LHC, and the associated technologies that allow for the con-
 583 trol and operation of the high-energy, high-luminosity beams that allow the CMS and ATLAS
 584 experiments to search for heavy particles and rare-processes.

585 3.1 The LHC Accelerator Complex

586 The main LHC ring is a 26.7 km tunnel, that is 45 m to 170 m underneath the surface of the
 587 earth, with 1.4% slope towards Lake Leman. It extends accross the French-Swiss border, into
 588 the French coutnryside. The tunnel was originally constructed between 1984 and 1989 for the
 589 Large Electron Positron (LEP) experiment that is famous for it's precision mesaurements of
 590 several Standard Model parameters [54]. The choice to build the ring underground was driven
 591 by real estate costs, but the underground setting also provides natural radiation shielding from
 592 the beamline and greatly reduces the impact of cosmic radiation on the detectors.

593 The LHC also utilizes the existing accelerator complex from the LEP experiment, which is
 594 shown in figure 3.3. The complex is composed a series of increasingly powerful accelerators that
 595 gradually increase the energy of the protons.

596 Protons are initially accelerated by the Linac2 linear accelerator up to 50 MeV [55] [56]. A

The LHC injection complex

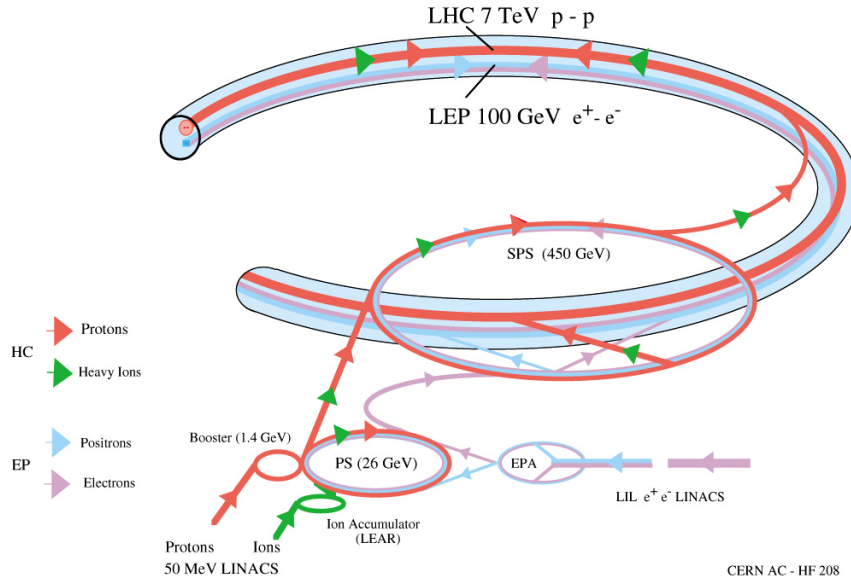


Figure 3.3: The LHC accelerator complex, taking protons from a bottle of Hydrogen at the Linac2, all the way to the LHC ring

597 bottle of Hydrogen is attached to a duoplasmatron source. This device ionizes the Hydrogen,
 598 and creates a 300 mA beam of protons, through a high-voltage anode, and a geometry designed
 599 to focus and collimate the beam as it leaves the device. Figure 3.4(a) shows a schematic for
 600 this device, showing the gas input on the left, and proton beam leaving to the right. Figure
 601 3.4(b) shows the actual device used in the Linac2 at CERN. The proton beam then enters
 602 the Radio-Frequency Quadropole (RFQ) system, which accelerates and bunches the protons
 603 up to 750 keV. The RFQ is a waveguide with four flanges, which have been machined with a
 604 sinusoidal modulation in the longitudinal direction, which creates an standing electric wave in
 605 this direction, accelerating the protons. Figure 3.4(c) shows a schematic of this modulation,
 606 and figure 3.4(d) is a close-up image of this modulation in an actual RFQ. The last stage of
 607 acceleration is provided by three Alvarez tanks. Each Alvarez tank holds a series of elctrically
 608 isolated cylinders, known as drift tubes, coaxial with the main tank, with gaps in between them.
 609 An alternating electric field is present in the gaps, and space between each drift tube and the
 610 walls of the tank. Protons passing through the center of the drift tubes feel no electric field, but
 611 the gaps are located such that, a proton will always see an accelerating field in the gap, and are
 612 thus receive a boost of energy from each gap as it traverses the length of the three tanks. Figure
 613 3.4(e) shows an image of the inside of an Alvaez tank, and figure 3.4(f) shows the tanks at the
 614 Linac2 at CERN. The final product is a 180 mA, 50 MeV proton beam, which is steered to the
 615 Proton Synchotron Booster for the next stage of acceleration.

616 The Proton Synchotron Booster (PS booster) complex accelerates the protons up to 1.4

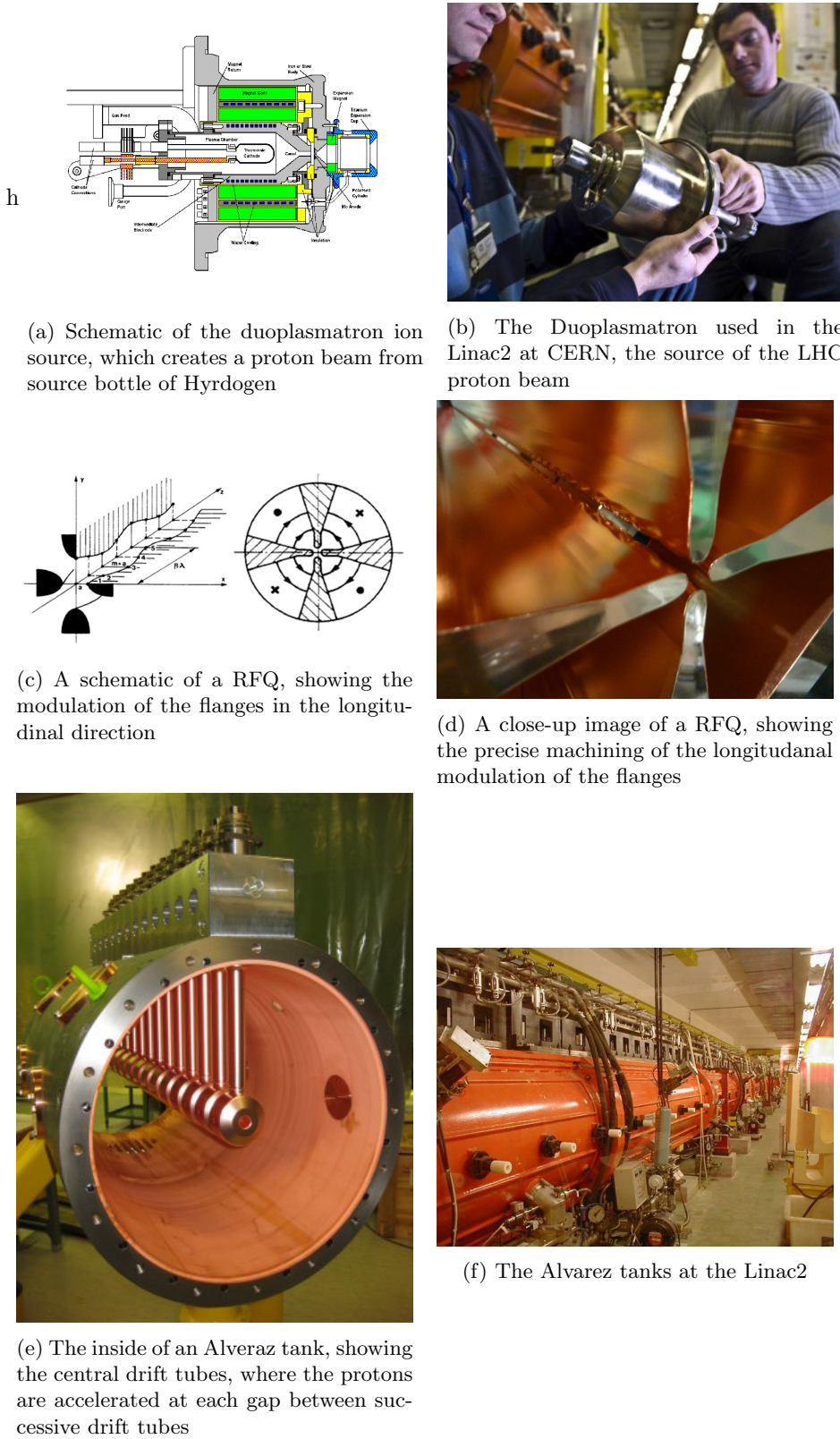


Figure 3.4: Features of the Linac2, the first stage of acceleration in the LHC injection chain

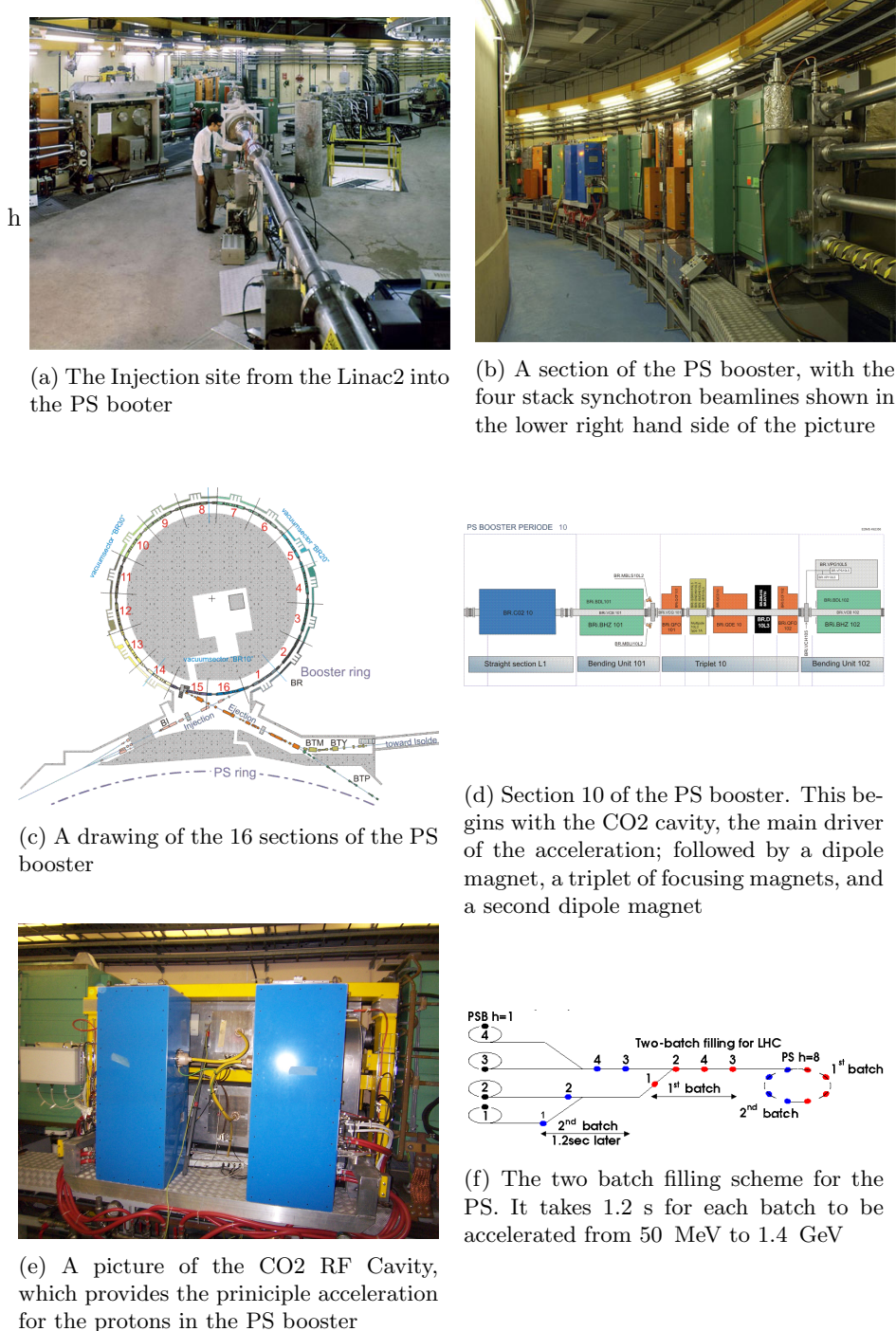


Figure 3.5: Features of the PS booster, the second stage of the LHC injection chain

617 GeV [55]. The complex takes the proton beam from the Linac2 and splits the beam into four
 618 separate, synchrotrons, stacked on top of one another. Figure 3.5(a) shows the injection site of
 619 the proton beam from the Linac2 into the PS booster. The right side of figure 3.5(b) shows the
 620 four synchotron beam pipes stacked vertically on top one another. The splitting of the beam is
 621 done in order to reduce the effect of the space charge of the proton beam, which would increase
 622 the transverse emmitance beyond a tolerable degree. The PS booster uses thirty-two 0.87 T
 623 dipole magnets to bend the beams, and fourty-eight quadrupoles to focus the beam as it makes
 624 its way around each of the 50 m diameter rings. Each magnet is composed of a vertical stack
 625 of four magnets, one for each of the synchotrons, and share a common yoke, allowing one power
 626 supply to provide the current to all of them in series [57]. The booster is divided into 16 arcs, as
 627 shown in figure 3.5(c). Each arc contains a bending dipole, 3 focusing quadrupoles, and a second
 628 bending dipole, followed by a straight section containing beam diagnostic, injection and ejection
 629 systems, and in three sections, the Radio-Frequency (RF) cavities, which is the mechanism of
 630 accelerating the beam [58]. Figure 3.5(d) shows the layout of the tenth arc, which also contains
 631 one of the RF cavities in the first section.

632 An RF cavity is a specially shaped, hollow conductor, that the beam passes through [59].
 633 The shape of the cavity determines the resonant frequency and harmonics (integer multiples of
 634 the fundamental frequency), of the standing electromagnetic fields that result when the cavity
 635 is driven by an alternating voltage source. The idea is to choose a resonant frequency such
 636 that the proton will always experience a positive electric field, and thus an acceleration, each
 637 time it passes through the RF cavity. This means that the revolution frequency of the proton
 638 must be equal to the fundamental frequency or harmonic of the RF cavity, $f_{RF} = n \times f_{rev}$, with
 639 $n = 1, 2, 3, \dots$. Eventually, the proton is accelerated up to an equilibrium speed and will enter the
 640 cavity just as the standing electric field is alternating through it's zero point. If arrives too early
 641 for this (moving too fast), then it will experience a negative electric force, a deceleration, which
 642 will eventually bring it back to the equilibrium revolution frequency, where it experiences zero
 643 net force. A diffuse beam of protons will be bunched into groups of protons through this effect
 644 as well, as the faster protons in the beams are decelerated, and the slower ones accelerated,
 645 until they all reach the same equilibrium revolution frequency. Driving the RF cavity with a
 646 harmonic, n , of the proton's revolution speed will thus create n bunches of protons. Each one of
 647 the potential n bunch positions is referred to as a bucket. In the case where a proton has to be
 648 accelerated through a wide range of energies, the frequency of the cavity must also increase to
 649 maintain synchronization with the proton revolution frequency.

650 Three types of RF cavities are used to accelerate the beam during each revolution. The first
 651 of the three types of RF cavities is the CO₂, with frequency range of 0.6 to 2.0 MHz and is used

652 to drive the $h = 1$ harmonic of the synchrotron, and is pictured in figure 3.5(e). The second
 653 type of cavity is the CO4 chamber, with a frequency range of 1.2 to 3.9 MHz, and drives the
 654 $h = 2$ mode of the synchrotron. This second mode is capable of splitting the beam and creating
 655 two separate bunch structures. However, for LHC running, only one bunch is used, and is driven
 656 primarily by the $h = 1$ mode. The $h = 2$ mode is supplemental and is used to shape the beam.
 657 A third type of RF cavity, CO16, has a frequency range of 5 to 16 MHz, and is used to control
 658 the longitudinal shape of a bunch during acceleration. The beam leaves the PS booster and enters
 659 the PS in a two-batch filling scheme, taking only 1.2 s to accelerate a second batch of protons
 660 from 50 MeV to 1.4 GeV. This second batch enters just as the first batch has traveled to the
 661 opposite side of the PS ring. A schematic of this process is shown in figure 3.5(f). To achieve
 662 the 25 ns bunch spacing design of the LHC, only 6 bunches of proton beam need to be delivered
 663 to PS. This is achieved by either using a 4+2 or 3+3 filling scheme, in terms of the number of
 664 proton bunches derived from the four possible synchotrons.

665 The next stage is the Proton Synchrotron (PS), which will boost the protons up to 25
 666 GeV [55]. The layout is shown in figure 3.6(a). The ring has a circumference of 628 m, and
 667 uses 100 dipole magnets and 177 higher-order focusing magnets, to steer the beam around the
 668 ring. Figure 3.6(b) shows a picture of one of the dipole magnets used at the PS. In addition
 669 to providing acceleration up to 25 GeV, the PS forms the basis of the bunch structure that is
 670 eventually used in the LHC. The $h = 7$ harmonic is used to capture the 6 bunches of protons
 671 delivered from the PS booster, leaving a gap in the place of a seventh bunch. The beam is then
 672 split into three, by using three different RF cavities tuned to the $h = 7, 14, 21$ modes of the PS.
 673 Figure 3.6(c) shows a simulation of a proton bunch being divided into three over the course of
 674 25 ms. The $h = 21$ mode is then used to accelerate the protons to from 1.4 to 25 GeV using the
 675 20 MHz RF cavity. Each bunch is then split twice, using the $h = 21, 42, 84$ synchroton modes,
 676 to create 72 bunches, spaced 25 ns apart, with a 320 ns gap for the 12 unused buckets of the
 677 $h = 84$ harmonic. This process is simulated in figure 3.6(d), over the course of 125 ms. The 320
 678 ns gap is created to account for the rise time of the kicker magnet, which ejects the beam out of
 679 the PS into the SPS. The entire splitting process is summarized in figure 3.6(e). For the case of
 680 50 ns bunch spacing, the final stage of splitting is not performed, and the $h = 21, 42$ modes are
 681 used to split the beam. Finally, in order to fit the bunches into the 200 MHz RF acceleration
 682 scheme of the SPS, the bunch length must be compressed from 11 ns to 4 ns. This is achieved
 683 by rotating the beam in the energy vs time phase space by sequential increases in voltage to
 684 the 40 MHz $h = 84$ mode, followed by an increase to the 80 MHz $h = 168$ mode. Figure 3.6(f)
 685 shows the result of this rotation - a distortion free ellipse with a smaller 4 ns spread, but a larger
 686 spread in the energy spectrum of the proton beam.

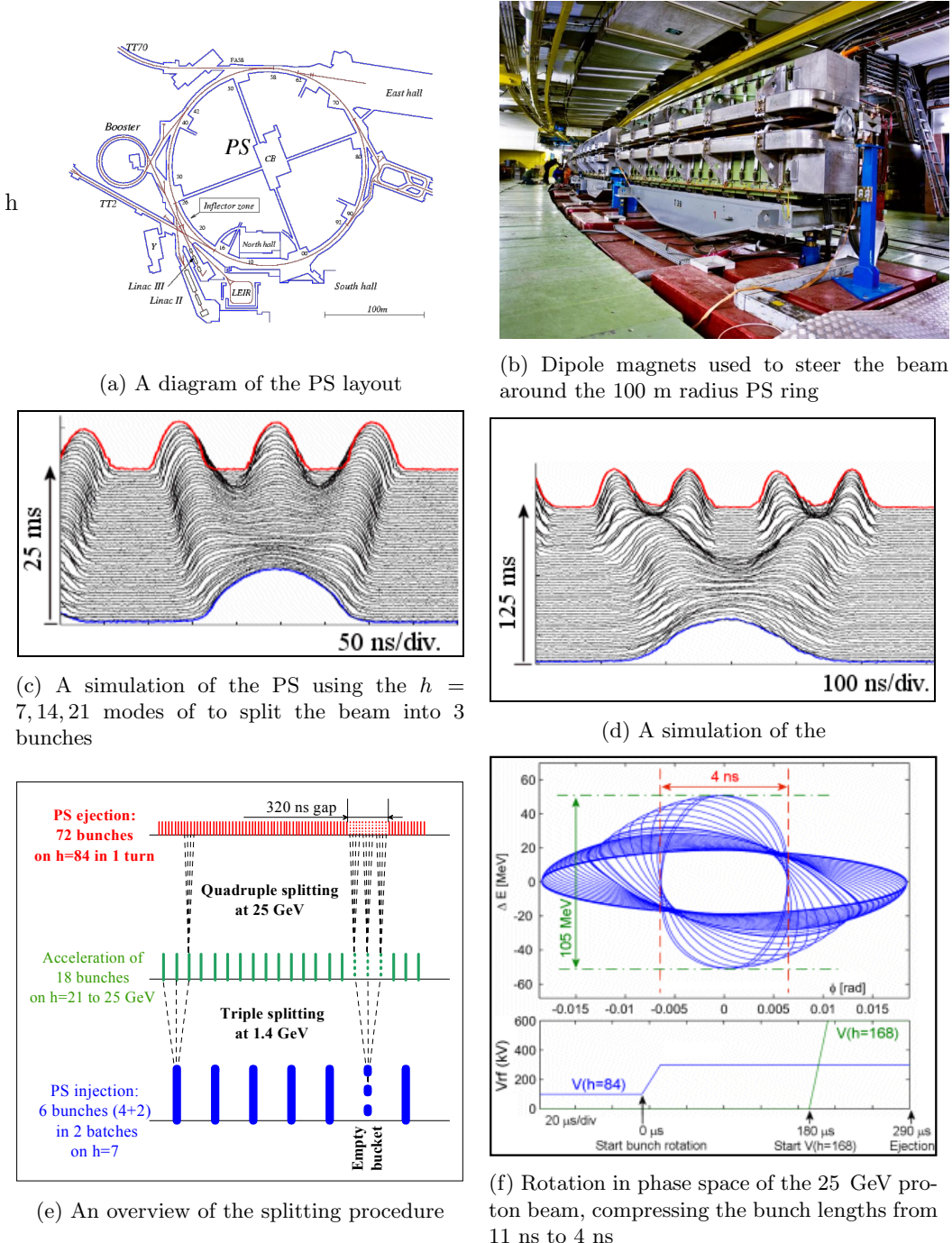


Figure 3.6: Features of the PS, the third stage of the LHC injection chain

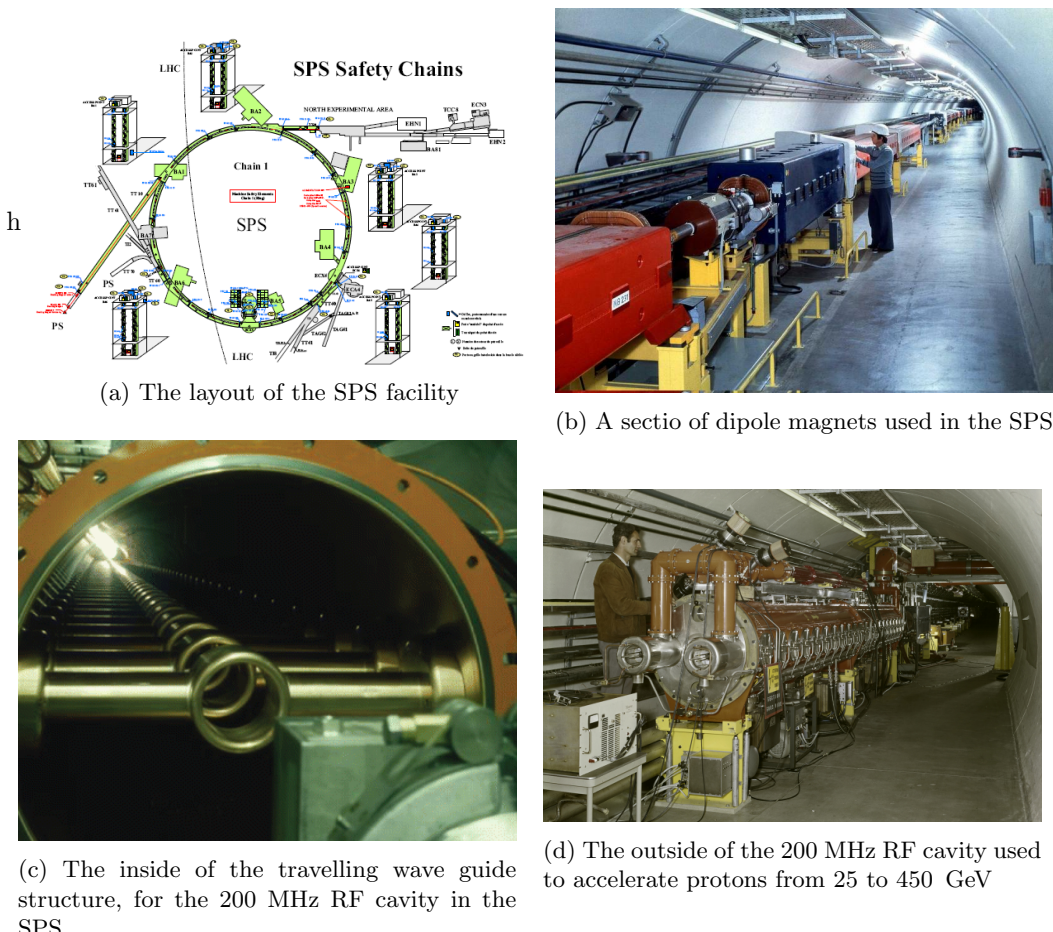


Figure 3.7: Features of the SPS, the fourth and final stage of the LHC injection chain

687 Next, the protons arrive at the Super Proton Synchotron (SPS), where they will be acceler-
 688 erated to 450 GeV. The SPS is the last stage of acceleration before the protons are injected
 689 into the LHC. The layout is show in figure 3.7(a). It has a circumference of 7 km, and steers
 690 the proton beam with 744 dipole magnets, with 573 higher-order focusing magnets [60]. Figure
 691 3.7(b) shows one of the dipole mangets in the SPS tunnel. Like all the other synchrotrons in
 692 the injection chain, the acceleration is provided by RF cavities. A 200 MHz system of RF cavi-
 693 ties capture and fill the SPS by using 2-4 batches of 72 bunch proton beams from the PS [55].
 694 Although the relative change in frequency is small, the large degree of acceleration necessitates
 695 the use of a tunable RF cavity. The 200 MHz system has 2 sections of 4 travelling wave cavities
 696 in series, and another 2 sections of 5 cavities in series. Figure 3.7(c) shows the insde of this
 697 structure, which uses drift tubes to accelerate protons in the gaps between tubes, with horzion-
 698 tally mounted bars, spaced 374 mm [61] apart, determining the periodicity of the resonant RF
 699 field that builds up inside. The outside of the structure is shown in figure 3.7(d). An additional
 700 800 MHz system is used to control the transverse emmitance. It is also used to stabalize the
 701 beam-line and prevent coupled-bunch instabilities [55].

702 Finally, protons are injected into the LHC ring in one clockwise, and another counter-
 703 clockwise rotating beams. In order to work in the limited space of the existing LEP tunnel,
 704 the two beams are contained within a single meachanical and cryostate structure, with a dual-
 705 bore design for each of the beams. Here, each proton beam is accelerated to their final energy of
 706 7 TeV, moving at 99.999991% the speed of light, before they meet head on, producing 14 TeV
 707 center-of-mass collisions.

708 The LHC ring itslef is divided into eight octants, with eight straight sections that are located
 709 in front and behind each of the eight collision points, where the beams are made to cross and
 710 collide, as shown in figure 3.8. These crossings are known as interaction regions (IRs). Four
 711 of these points are currently being used by experiments. TOTEM has detectors on either side
 712 of the CMS experiment at one interaction region, known as point 5 (P5). LHCf has detectors
 713 on either side of ATLAS at point 1 (P1). MOeDAL has detectors near LHCb at point 8 (P8)
 714 and the ALICE detector is located at point 2 (P2). The following sections will cover the RF,
 715 magnet, cryogen, and vaccuum technologies used in the LHC ring.

716 3.2 LHC Magnets

717 Several types of magnets are used in order to properly circulate and focus the proton beam as
 718 it makes its way around the 26.7 km long tunnel. A complete list of all types, can be found in
 719 the technical design report [62], as well as through CERN's outreach web resources [63]. This

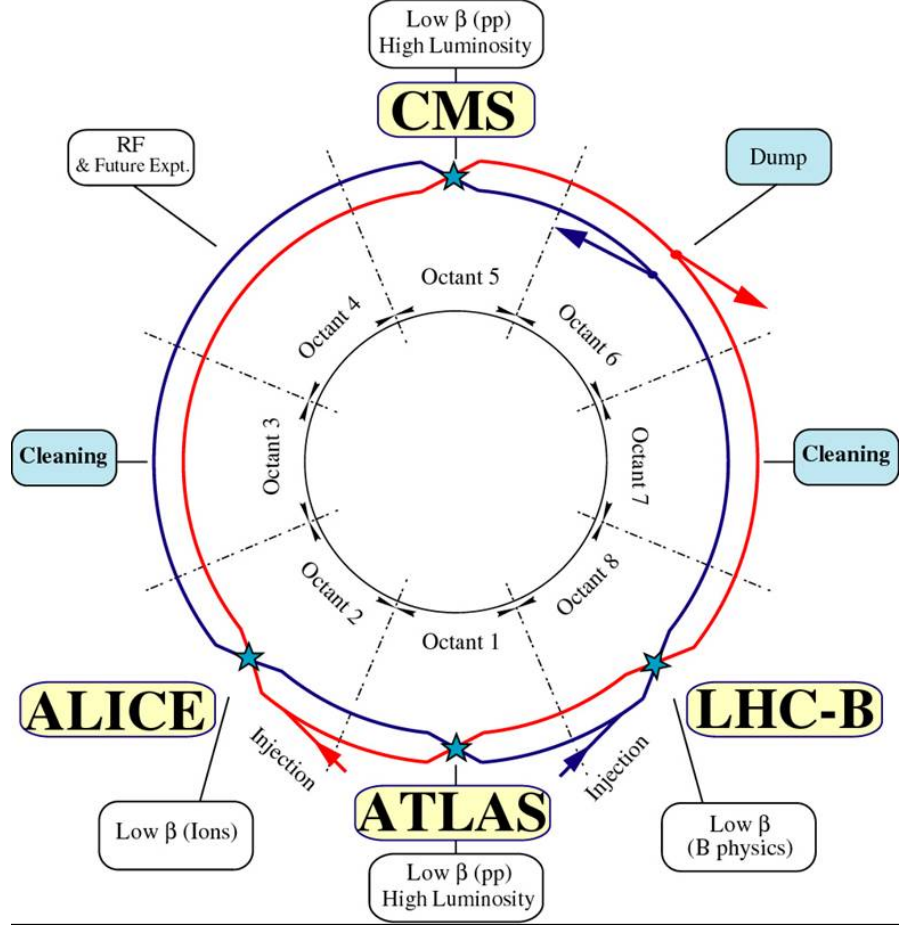


Figure 3.8: The LHC ring is divided into eight octants

section will give an overview of the a few of the critical subsystems: the septum and kicker magnets used for injection from the SPS, the dipole magnets used for bending the beam around the circumference of the ring, and the higher-order-pole magnets that are used for focusing the beam.

The injection and extraction of proton beams from one synchrotron to another involves three types of magnets, septums, kickers, and bumpers. Septum magnets contain a partition, or a septum, that provides a boundary between a high magnetic field region and a near-zero magnetic field region and are operated in DC or a slow-pulsed mode [64]. In case of injecting a beam of protons into a synchrotron, the target beampipe of the synchrotron passes through the low-field region, so the trajectory is unaffected by the high-field region, which bends the injection beam towards the synchrotron aligning it horizontally, with the target beam. The kicker magnet, is a fast-pulsed magnet and provides the timing selection in order to make a final bend vertical bend into the synchrotron orbit, and into the correct basket of the synchrotron bunch train [65]. Finally, bumper magnets make small bends to the beam and align it with the injection site. Figure 3.9 shows a schematic for this process, where a transfer line brings protons to a septum, which bends the beam to a kicker, which makes the final corrections to match the synchrotron

Single-turn injection

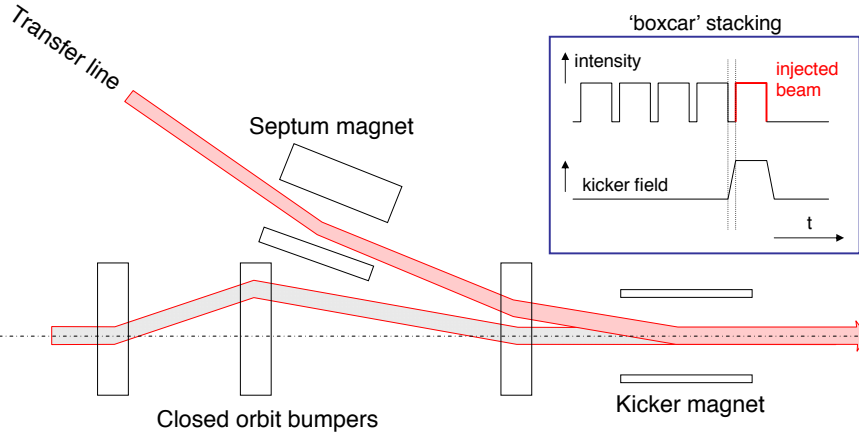


Figure 3.9: The single turn injection scheme. A septum magnet makes the initial alignment. The kicker magnet times the injection and makes the final alignment. Bumper magnets align the LHC beam with the injected beam.

736 orbit. For extraction, the kicker magnet quickly displaces a portion of the beam, which is steered
 737 away by the septum, while the original beam passes through its low-field region unaffected.

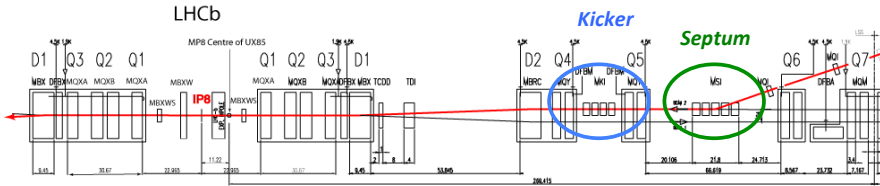


Figure 3.10: Layout of Interaction Region 8, where one proton beam is injected into the LHC ring. A transfer line from the SPS brings a proton in from the right. In green, a septum magnet aligns the beam horizontally with the LHC. In blue, a kicker magnet makes the final vertical alignment into the LHC, and is timed to fill one of the 400 MHz buckets of the RF capture system

738 At the LHC, beam is injected at Interaction Regions (IR) 2 and 8 [54]. Two transfer lines
 739 bring the beam extracted from the SPS to ~ 150 m of the LHC ring. Five Labertson-type septum
 740 magnets, of field strength ~ 1 T, are used to deflect each of the transfer line beams 12 mrad
 741 to align the transfer beam horizontally with the LHC orbit. Then, four ~ 0.12 T MKI kicker
 742 magnets quickly deflect the beam 0.85 mrad to close the orbit with the LHC ring. Figure 3.10
 743 shows the layout of the injection point at IR 8. The green circle encloses the septum structure,
 744 which provides the horizontal alignment, and the blue encloses the kicker structure, which makes
 745 the final vertical alignment and synchronizes the injection of the beam into the LHC. The rise
 746 time for the field provided by the kicker magnets in the LHC and SPS determine the final bunch
 747 structure of the LHC. Figure 3.11 extends figure 3.6(e) showing how the rise times of the kickers
 748 that inject, or eject beam create gaps in the bunch structure of the LHC. The initial filling of the
 749 PS with 6 batches of protons from the PSB, leaves one initial bucket unused in the PS. After

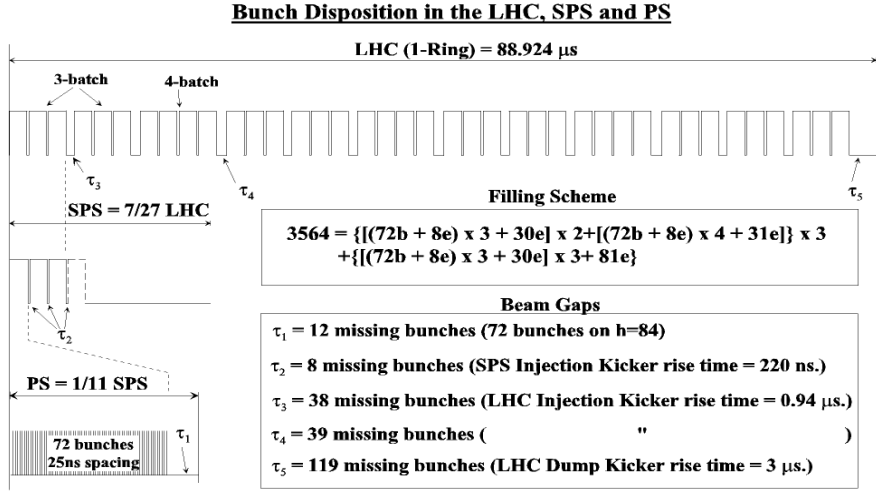


Figure 3.11: The initial filling of 6 batches of protons from the PSB to the PS, leaves 12 empty buckets in the PS bunch structure. The rise time of the SPS magnet creates an additional gap in the SPS bunch structure. Additional gaps emerge due to the rise time of the LHC injection and dumping kicker magnets

750 the splitting of the beam into the 25 ns bunches, there 12 empty buckets at the of the PS bunch
 751 train. The SPS is filled with three to four of these trains, leaving an additional 8 25 ns buckets
 752 unfilled due to the 220 ns rise time of the SPS kicker magnet. These three to four trains are
 753 then injected into the LHC, where there are 38 or 39 bunch gaps due to the LHC injector 0.94
 754 μs rise time. At the end of a full LHC orbit, 119 buckets are left empty to allow for the rise time
 755 of the beam dumping kicker magnet, used to remove beam from the LHC.

756 Once the beam is injected, the curved path around the circumference of the LHC is main-
 757 tained via 1232 superconducting dipole magnets. The superconducting material niobium-titanium,
 758 NbTi, is cooled to 1.9 K in order to produce the 8.33 T field. Figure 3.12(a) shows a cross-section
 759 view of one of the LHC dipoles. The dual-bore design of the beam-pipe is enclosed by an iron
 760 yoke, that serves as the cold mass to maintain the superconducting temperature, and provides
 761 a 195 mm gap between each beam. A close up picture of the non-magnetic collar and supercon-
 762 ducting coils are shown in figure 3.12(b). A simulation of the magnet in figure 3.12(c) shows the
 763 homogenous, vertical magnetic field produced in the center of the coil. Diagram 3.12(d) shows
 764 an exaggerated view of the 2812 m radius curvature of each dipole. However, since each dipole
 765 is only ~ 14 m in length, this curvature is hardly noticeable, as shown in a photo of an actual
 766 dipole magnet in a staging area at CERN, awaiting installation in figure ??(e).

767 Quadrupole, septupole, octupole, and other multipole magnets are used to focus a single
 768 beam, as well as squeeze the two beams together. There are 392 quadrupole magnets on the
 769 LHC ring, each controlling the height and width of the beam. Figure 3.13(a) shows a schematic
 770 of a dual-bore quadrupole magnet, and figure 3.13(b) shows an actual quadrupole in a staging
 771 area before installation. Quadrupole magnets use four sets of coils to create a magnetic field that

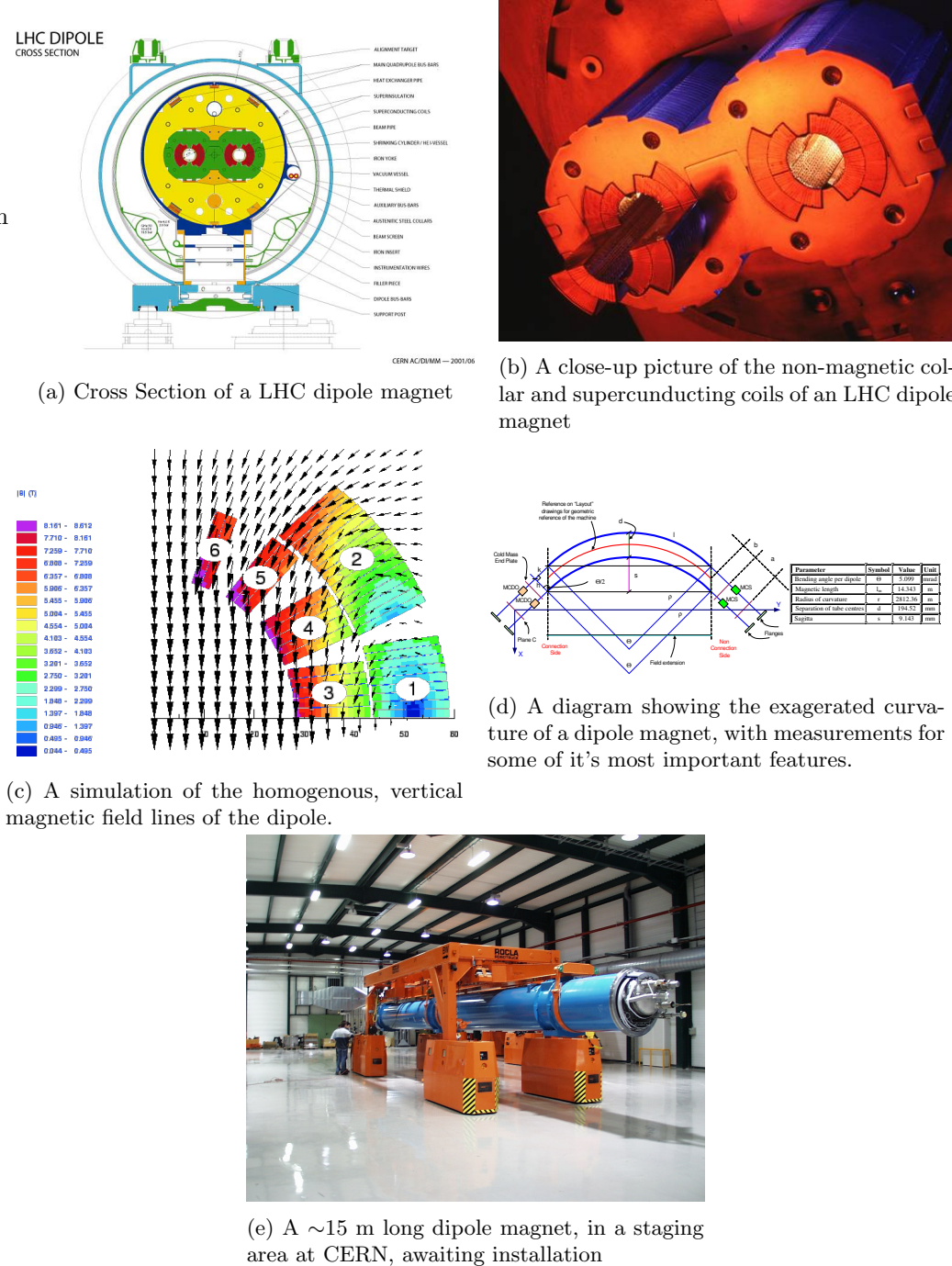
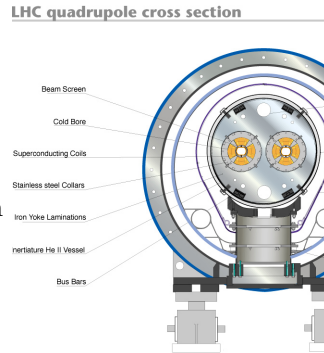


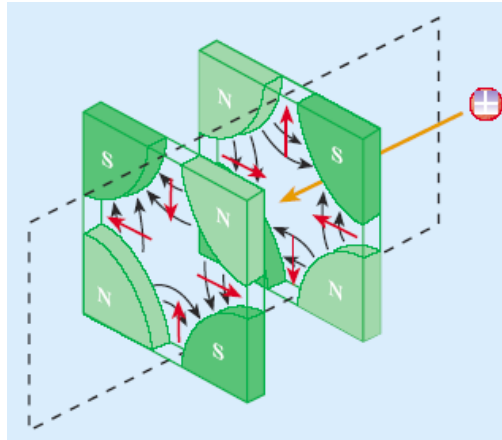
Figure 3.12: Features of the dipole magnets used in the LHC



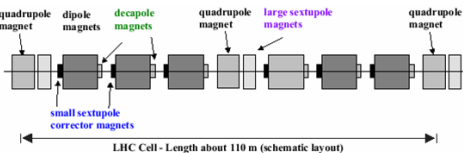
(a) Cross Section of a LHC quadrupole magnet



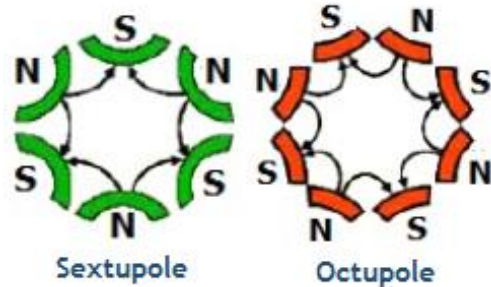
(b) A dual-bore quadrupole magnet, in a staging area prior to installation



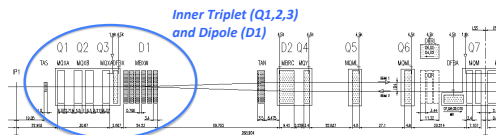
(c) A quadrupole magnet can provide focusing either in the horizontal or vertical direction



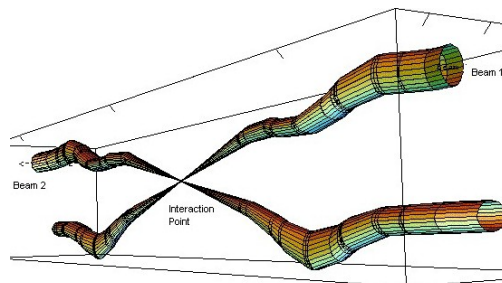
(e) A typical 110m long magnetic cell at the LHC featuring several types of multipole magnets



(d) Multipole fields from a sextupole and an octupole magnet



(f) Schematic of the Inner triplet structure that brings the two separate beams together in the interaction region



(g) A simulation of two beams being squeezed together by the inner triplet.

Figure 3.13: Features of the dipole magnets used in the LHC

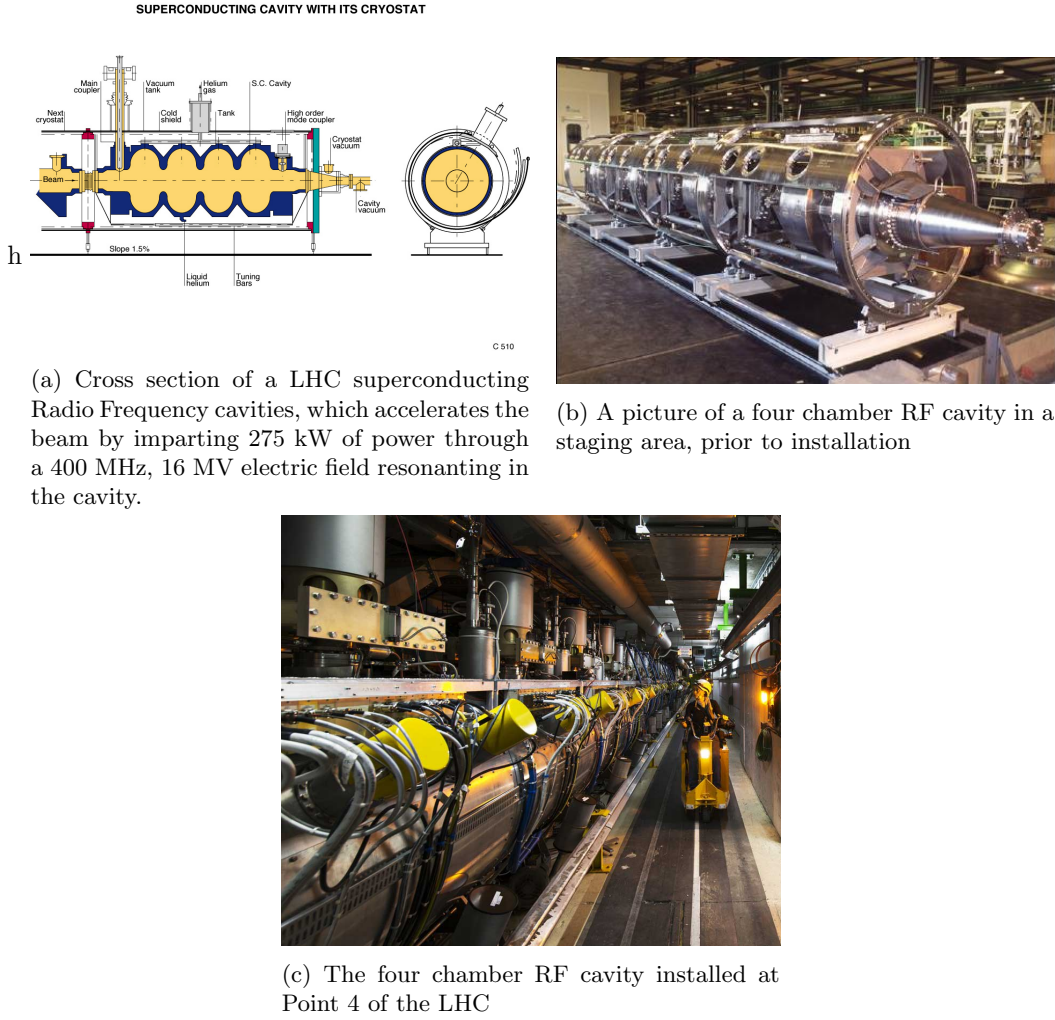


Figure 3.14: Features of the 400 MHz superconducting RF system used in the LHC

either squeezes the beam horizontally or vertically, as shown in figure 3.13(c). Finer corrections to the beam shape are made with the multipole magnets, since they are able to compress the beam from more than two axes. Figure 3.13(d) shows the fields lines of a sextupole and octupole magnet. A typical cell of magnets, 110 m long, in the LHC beamline is shown in a diagram in figure 3.13(e), where the dipole, quadrupole and higher order magnet work in series to confine the protons to the LHC ring. Finally, a set of single bore magnets, known as an inner triplet, bring the two beams together into an interaction region. Figure 3.13(f) shows the arrangement of magnets that squeeze the beam together, while figure 3.13(g) shows a simulation of the beams being brought together to collide in the interaction region.

3.3 LHC RF Technology

The LHC uses a 400 MHz superconducting RF cavity system to capture and accelerate the beam from 450 GeV to 7 TeV [54]. Two independent system are used to provide 8 MV of RF voltage

at injection at 16 MV during equilibrium at 7 TeV and deliver 275 kW of power to each beam. This is provided by 16 niobium sputtered cavities, housed in 4.5 K refrigeration units, known as cryomodules, at Point 4 of the LHC octant. The superconducting material covering the inside of the cavity has near-zero resistivity, which dissipates much less power and has a much narrower resonance width, or Q-factor, than a cavity made from normally conducting material. Figure 3.14(a) shows a schematic of a four cavity cryomodule. The beam pipe passes through the center of each chamber and longitudinal (left to right in the diagram) electric fields accelerate the protons each time they circulate the LHC ring. Figure 3.14(b) shows an actual four cavity module in a staging area prior to installation. In this picture, the resonance cavities are concealed underneath the cylindrical housing of the vacuum tank and cryostat. Figure 3.14(??) is a picture of the module installed at Point 4. The thin cylindrical structures extending off the top is the LHe intake valve and quench system. The thicker cylindrical structures are the waveguides that couple the cavities to the source of the electric field, the klystrons.

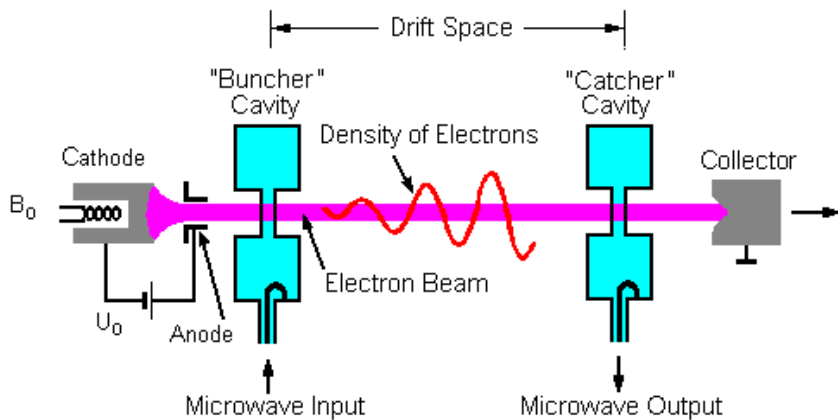


Figure 3.15: A klystron uses a weak RF signal coupled to a resonance cavity to bunch an electron beam, which in turn creates an amplified RF signal as it passes through a second resonance cavity tuned to the same frequency.

A Klystron is the source of RF power that builds up as a resonance in the cavities that accelerate the protons. Figure 3.15 shows a diagram of the basic operating principle. The device uses an anode to accelerate the thermionic emission of electrons off of a cathode material into one or more bunching cavities tuned to the frequency the device is designed to produce. This cavity is driven with a weak RF source, that groups electrons into bunches. Just as discussed for protons earlier, when electrons arrive at the entrance of the cavity at just the right time, it will experience the zero-point of the oscillation of the resonating electric field. If it arrives early or late, it is accelerated or decelerated and thus bringing it closer to its neighbors, and increasing the density of the beam. After passing through multiple chambers, the tightly bunched electrons enter a catcher cavity tuned to the same resonance frequency. As the electrons pass through at

807 this resonance frequency, standing electric waves are excited and quickly build up in the catcher
 808 cavity. The electron beam is thus used to amplify the original RF signal in the catcher cavity,
 809 which is then transported via waveguide to power the RF cavity used to accelerate the proton
 810 beamline.

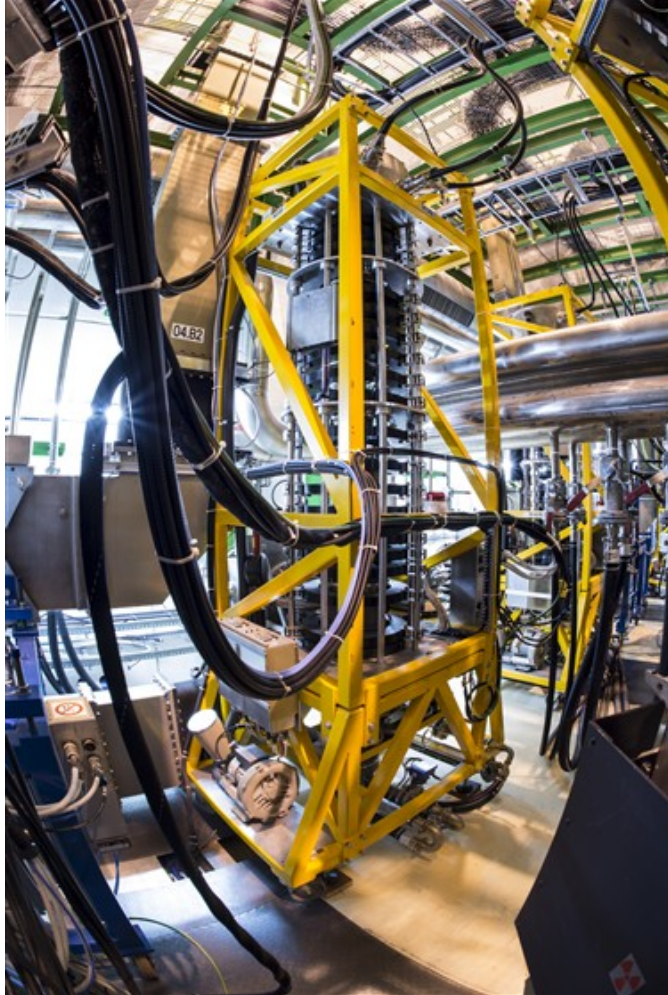


Figure 3.16: One of sixteen 300 kW, 400 MHz klystrons that power the superconducting RF cavities that accelerate the proton beam.

811 At the LHC, 16 400 MHz, 300 kW kylstrons, work together to provide 4800 kW of power
 812 to the superconducting RF cavities [54]. They are also located at Point 4, in the UX45 service
 813 cavern adjacent to the RF cavities, about 6 m below the beamline. An average of 22 m of
 814 waveguide is used to transport the power generated by the kylstrons to the RF cavities. Figure
 815 3.16 shows a kylstron installed at the LHC, and like most modern kylstrons, it also utilizes a
 816 multi-bunching chamber design.

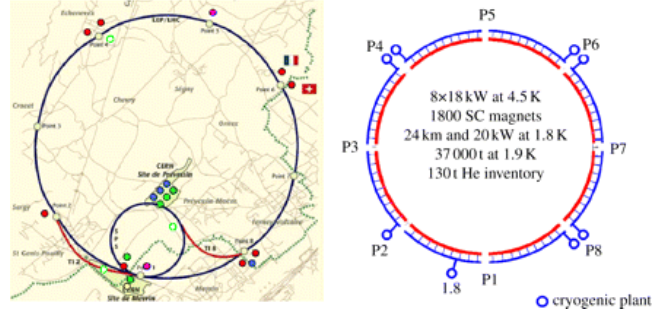


Figure 3.17: Layout of the five cryogenic islands, which are home to the eight facilities that provide liquid helium to the LHC



(a) The compressor station for the 4.5 K refrigeration system

(b) The 4.5 K refrigeration system cold box, containing heat exchanging fins and turbines to cool the He

Figure 3.18: Features of the 4.5 K refrigeration system

3.4 The LHC Cryogen System

The LHC is the largest cryogenic system in the world [66], as its operating temperature is 1.8 K, in order to produce the high-magnetic fields needed by the dipole magnets. Additionally, the acceleration mechanism, the RF cavities, are also superconducting, and must be cooled to 4.5 K. Over 120 tons of Helium are used as the cryogenic medium, since once it is cooled below 2.17 K, it becomes a superfluid, a phase of matter with a high thermal conductivity, making it ideal for refrigeration. Cryogenic and auxiliary equipment are concentrated into 5 cryogenic islands at Points 1, 2, 4, 6, and 8 [54]. As shown in figure 3.17, Point 4, 6, and 8 house two facilities each, making a total of eight, one for each octant of the LHC arc.

At each cryogenic plant, He is cooled to 80 K by circulating it through refrigeration equipment with liquid nitrogen in the heat exchangers [66]. Next, the He is brought to 4.5 K with refrigerators recovered from the LEP experiment [67]. The He gas is first compressed and allowed to expand, where it is cooled by losing energy through mechanical turbo-expanders that run at up to 140,000 rpm on helium-gas bearings. Figure 3.18(a). The He is then liquified after passing through a vacuum sealed box containing heat exchangers and more turbo-expanders [68].

832 The compressor for this system is pictured in figure 3.18(b). Finally, the liquified He is brought
 833 to 1.8 K with a refrigeration unit that uses a cold compression train to decrease the saturation
 834 pressure, and thus temperature as well.

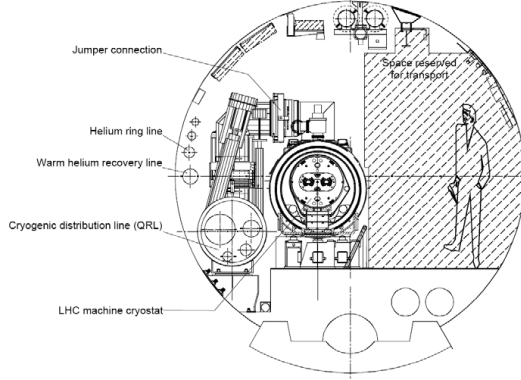


Figure 3.19: Cross section schematic of the cryogenic distribution system in the LHC tunnel

835 In the LHC tunnel, a cryogenic distribution line runs parallel to the machine [67]. It consists
 836 of eight 3.2 km long cryostats, that contain the equipment to supply and recover helium with
 837 temperatures ranging from 4 K to 75 K. A total of 310 service modules, are used to control the
 838 system and provide safety mechanisms against pressure buildup and magnet quenching. Figure
 839 shows a cross section of the cryogen distribution system in the tunnel.

840 3.5 The LHC Vacuum System

841 The LHC is also the largest operational vacuum system in the world and is capable of achieving
 842 pressures lower than outer space [69]. Three different types of vacuum systems are used: one for
 843 insulating the helium distribution lines, another for insulating the dipole magnets, and a final
 844 ultra-high vacuum system for the beam pipe [54].

845 The vacuum systems for insulating the helium distribution and dipoles involves some 104 km
 846 of piping an over 250,000 welding joints [69]. Pressure here is required to be kept at 10^{-1} mbar,
 847 but at cryogenic temperatures, pressures tend to equalize at a much lower level, to 10^{-6} mbar
 848 ($\sim 10^{-9}$ atm) [54].

849 The most stringent requirements come on the vacuum of the beam-pipe. The beam must
 850 minimize the number of interactions it has with any particles outside of the interaction region.
 851 A pressure of 10^{-10} to 10^{-11} mbar are maintained in the 54 km of beampipe [69]. Weeks of
 852 cryogenic pumping, eventually condenses gas trapped in the beampipe into a liquid that can be
 853 absorbed by the walls of the beampipe. The inside beampipe is also coated with a thin layer



Figure 3.20: Beam screen for the LHC, with slits to allow for easy pumping of residual gas molecules in the beampipe.

of a special substance developed at CERN, a titanium-zirconium-vanadium alloy, which absorbs residual particles when heated. 780 ion pumps are used to remove the noble gases and methane, which do not interact with the substance, which acts as its own distributed pumping system. Room-temperature sections of the beampipe are also heated to 300^{deg} to be baked-out from the outside. This is done to periodically remove any material which may have settled and become trapped. Additionally, the beam-pipe is designed with a racetrack shape, which optimises the available aperture while leaving space for the cooling tubes, as shown in figure 3.20. Slits also allow for gas molecules to be easily pumped out from inside its volume.

⁸⁶² Chapter 4

⁸⁶³ The Compact Muon Solenoid

⁸⁶⁴ The Compact Muon Solenoid (CMS) is one of two general purpose detectors at the LHC.

⁸⁶⁵ 4.1 The Inner Tracker

⁸⁶⁶ The inner tracker is silicon and really really big, lots of channels.

⁸⁶⁷ 4.2 The Electromagnetic Calorimeter

⁸⁶⁸ PbWO₄ crystals. APDs in the Barrel. VPTs in the Endcaps

⁸⁶⁹ 4.2.1 Vacuum Photo-Triodes

⁸⁷⁰ Extra time for VPTs

⁸⁷¹ 4.2.2 Test Rig at UVa

⁸⁷² Big magnet, lots of light, test dem led's

⁸⁷³ 4.2.3 Results of UVa Tests

⁸⁷⁴ Plots, Plots, plots, plots, plots

⁸⁷⁵ 4.3 The Hadronic Calorimeter

⁸⁷⁶ Brass, Steel, Soviet Sweat

877 4.4 Forward Calorimetry

878 High eta, great for VBF

879 4.5 Magnet and Return Yoke

880 Describe solenoid and measuring field, and engineering marvel or return yoke structure.

881 4.6 Muon Chambers

882 APDs DTs and CSCs

883 4.7 Data Collection Overview

884 L1 trigger, HLT etc

885 **Chapter 5**

886 **Particle Reconstruction at CMS**

887 Data is reconstructed at CMS using the *ParticleFlowTM* algorithm

888 **5.1 Muon Reconstruction**

889 Muons rely heavily on the inner tracker and muons chambers for efficient identification and
890 reconstruction

891 **5.2 Electron Reconstruction**

892 Electrons leave charged tracks in the inner tracker, and create a wide shower of particles and
893 thus energy deposits in the ECAL. High energy electrons sometimes traverse the entire distance
894 of the ECAL and leave energy in the HCAL, however the ratio of these two energies is dispro-
895 portionate for the ECAL, and thus this ratio is often used to discriminate electrons from highly
896 electromagnetic hadronic jets.

897 **5.3 Photon Reconstruction**

898 Like electrons, but with no tracks, and narrower shower shape.

899 **5.4 Jet Reconstruction**

900 Jets are formed by matching tracks from the inner tracker to energy deposits in the ECAL
901 and HCAL. Energy clusters are identified from the ECAL and HCAL, and everything is then
902 clustered in a cone.

5.5 Tau Reconstruction

So heavy that they decay to leptons or hadrons before traversing the detector, they still leave an oddly-numbered pronged decay hadronically due to charge conservation requiring that one of the hadrons produced be equal charge to the tau. This results in one charged, and any number of neutral pions, or three charged, and any number of neutral pions.

5.6 Missing Transverse Energy Reconstruction

since the detector is hermetic, and the tracker so granular, we can ensure that no particles flew out of the detector due to lack of coverage. Only long-lived neutral particles can escape, such as neutrinos in the standard model. Many BSM theories, such as SUSY, are characterized by stable, neutral particles.

MET is the vector sum of all of the tracks associated with a particular primary vertex (?) or all vertices in event). Thus if there was a neutral particle that escaped detection, there would be a momentum imbalance along the trajectory of that particle. This is how neutrinos are identified.

Bibliography

- [1] “LHC Aerial View”.
URL <http://www.coepp.org.au/files/coepp/images/cern-aerial2.jpg>.
- [2] CMS Collaboration, “Observation of a new boson at a mass of 125 GeV with the CMS experiment at the LHC”, *Phys.Lett.B* (2012) [arXiv:1207.7235](#).
- [3] ATLAS Collaboration, “Observation of a new particle in the search for the Standard Model Higgs boson with the ATLAS detector at the LHC”, *Phys.Lett.B* (2012) [arXiv:1207.7214](#).
- [4] M. E. Peskin and D. V. Schroeder, “An Introduction to Quantum Field Theory”.
Westview Press, URL <http://www.westviewpress.com>, 1995.
- [5] K. G. Wilson, “Renormalization Group and Critical Phenomena. I. Renormalization Group and the Kadanoff Scaling Picture”, *Phys. Rev. B* **4** (Nov, 1971) 3174–3183, doi:[10.1103/PhysRevB.4.3174](https://doi.org/10.1103/PhysRevB.4.3174).
- [6] K. G. Wilson, “Renormalization Group and Critical Phenomena. II. Phase-Space Cell Analysis of Critical Behavior”, *Phys. Rev. B* **4** (Nov, 1971) 3184–3205, doi:[10.1103/PhysRevB.4.3184](https://doi.org/10.1103/PhysRevB.4.3184).
- [7] S. Bethke, “The 2009 World Average of alpha(s)”, *Eur.Phys.J.* **C64** (2009) 689–703, doi:[10.1140/epjc/s10052-009-1173-1](https://doi.org/10.1140/epjc/s10052-009-1173-1), [arXiv:0908.1135](#).
- [8] H. Weyl, “The theory of groups and quantum mechanics”. Dover Press,
URL <https://ia700807.us.archive.org/20/items/ost-chemistry-quantumtheoryofa029235mbp/quantumtheoryofa029235mbp.pdf>, 1930.
- [9] C. N. Yang and R. L. Mills, “Conservation of Isotopic Spin and Isotopic Gauge Invariance”, *Phys. Rev.* **96** (Oct, 1954) 191–195, doi:[10.1103/PhysRev.96.191](https://doi.org/10.1103/PhysRev.96.191).
- [10] M. Gell-Mann, “A Schematic Model of Baryons and Mesons”, *Phys.Lett.* **8** (1964) 214–215, doi:[10.1016/S0031-9163\(64\)92001-3](https://doi.org/10.1016/S0031-9163(64)92001-3).

- 941 [11] G. Zweig, “An SU₃ model for strong interaction symmetry and its breaking; Version 1”,
 942 Technical Report CERN-TH-401, CERN, Geneva, Jan, 1964.
- 943 [12] G. Zweig, “An SU₃ model for strong interaction symmetry and its breaking; Version 2”,.
- 944 [13] O. W. Greenberg, “Spin and Unitary-Spin Independence in a Paraquark Model of Baryons
 945 and Mesons”, *Phys. Rev. Lett.* **13** (Nov, 1964) 598–602,
 946 doi:10.1103/PhysRevLett.13.598.
- 947 [14] P. Higgs, “Broken symmetries, massless particles and gauge fields”, *Physics Letters* **12**
 948 (1964), no. 2, 132 – 133, doi:[http://dx.doi.org/10.1016/0031-9163\(64\)91136-9](http://dx.doi.org/10.1016/0031-9163(64)91136-9).
- 949 [15] S. Weinberg, “A Model of Leptons”, *Phys. Rev. Lett.* **19** (Nov, 1967) 1264–1266,
 950 doi:10.1103/PhysRevLett.19.1264.
- 951 [16] S. L. Glashow, “Partial-symmetries of weak interactions”, *Nuclear Physics* **22** (1961),
 952 no. 4, 579 – 588, doi:[http://dx.doi.org/10.1016/0029-5582\(61\)90469-2](http://dx.doi.org/10.1016/0029-5582(61)90469-2).
- 953 [17] A. Salam and J. Ward, “Electromagnetic and weak interactions”, *Physics Letters* **13**
 954 (1964), no. 2, 168 – 171, doi:[http://dx.doi.org/10.1016/0031-9163\(64\)90711-5](http://dx.doi.org/10.1016/0031-9163(64)90711-5).
- 955 [18] Nobelprize.org, “The Nobel Prize in Physics 1957”.
 956 URL http://www.nobelprize.org/nobel_prizes/physics/laureates/1957/.
- 957 [19] N. Cabibbo, “Unitary Symmetry and Leptonic Decays”, *Phys. Rev. Lett.* **10** (Jun, 1963)
 958 531–533, doi:10.1103/PhysRevLett.10.531.
- 959 [20] M. Kobayashi and T. Maskawa, “CP Violation in the Renormalizable Theory of Weak
 960 Interaction”, *Prog.Theor.Phys.* **49** (1973) 652–657, doi:10.1143/PTP.49.652.
- 961 [21] G. Arnison et al., “Experimental observation of isolated large transverse energy electrons
 962 with associated missing energy at s=540 GeV”, *Physics Letters B* **122** (1983), no. 1, 103
 963 – 116, doi:[http://dx.doi.org/10.1016/0370-2693\(83\)91177-2](http://dx.doi.org/10.1016/0370-2693(83)91177-2).
- 964 [22] G. Arnison et al., “Experimental observation of lepton pairs of invariant mass around 95
 965 GeV/c² at the {CERN} {SPS} collider”, *Physics Letters B* **126** (1983), no. 5, 398 – 410,
 966 doi:[http://dx.doi.org/10.1016/0370-2693\(83\)90188-0](http://dx.doi.org/10.1016/0370-2693(83)90188-0).
- 967 [23] M. Banner et al., “Observation of single isolated electrons of high transverse momentum
 968 in events with missing transverse energy at the {CERN} pp collider”, *Physics Letters B*
 969 **122** (1983), no. 56, 476 – 485,
 970 doi:[http://dx.doi.org/10.1016/0370-2693\(83\)91605-2](http://dx.doi.org/10.1016/0370-2693(83)91605-2).

- 971 [24] P. Bagnaia et al., “Evidence for Z0e+e at the {CERN} pp collider”, *Physics Letters B*
 972 **129** (1983), no. 12, 130 – 140,
 973 doi:[http://dx.doi.org/10.1016/0370-2693\(83\)90744-X](http://dx.doi.org/10.1016/0370-2693(83)90744-X).
- 974 [25] The ALEPH, DELPHI, L3, OPAL, SLD Collaborations, the LEP Electroweak Working
 975 Group, the SLD Electroweak and Heavy Flavour Groups, “Precision Electroweak
 976 Measurements on the Z Resonance”, *Phys. Rept.* **427** (2006) 257,
 977 [arXiv:hep-ex/0509008](https://arxiv.org/abs/hep-ex/0509008).
- 978 [26] The ALEPH, DELPHI, L3, OPAL Collaborations, the LEP Electroweak Working Group,
 979 “Electroweak Measurements in Electron-Positron Collisions at W-Boson-Pair Energies at
 980 LEP”, *Phys. Rept.* **532** (2013) 119, [arXiv:1302.3415](https://arxiv.org/abs/1302.3415).
- 981 [27] F. Abe et al., “Observation of Top Quark Production in $\bar{p}p$ Collisions with the Collider
 982 Detector at Fermilab”, *Phys. Rev. Lett.* **74** (Apr, 1995) 2626–2631,
 983 doi:[10.1103/PhysRevLett.74.2626](https://doi.org/10.1103/PhysRevLett.74.2626).
- 984 [28] S. Abachi et al., “Search for High Mass Top Quark Production in $p\bar{p}$ Collisions at $\sqrt{s} =$
 985 1.8 TeV”, *Phys. Rev. Lett.* **74** (Mar, 1995) 2422–2426,
 986 doi:[10.1103/PhysRevLett.74.2422](https://doi.org/10.1103/PhysRevLett.74.2422).
- 987 [29] LHC Higgs Cross Section Working Group Collaboration, “Handbook of LHC Higgs Cross
 988 Sections: 3. Higgs Properties”, doi:[10.5170/CERN-2013-004](https://doi.org/10.5170/CERN-2013-004), [arXiv:1307.1347](https://arxiv.org/abs/1307.1347).
- 989 [30] W. Beenakker et al., “Higgs radiation off top quarks at the Tevatron and the LHC”,
 990 *Phys.Rev.Lett.* **87** (2001) 201805, doi:[10.1103/PhysRevLett.87.201805](https://doi.org/10.1103/PhysRevLett.87.201805),
 991 [arXiv:hep-ph/0107081](https://arxiv.org/abs/hep-ph/0107081).
- 992 [31] W. Beenakker et al., “NLO QCD corrections to t anti-t H production in hadron
 993 collisions”, *Nucl.Phys.* **B653** (2003) 151–203, doi:[10.1016/S0550-3213\(03\)00044-0](https://doi.org/10.1016/S0550-3213(03)00044-0),
 994 [arXiv:hep-ph/0211352](https://arxiv.org/abs/hep-ph/0211352).
- 995 [32] R. Frederix et al., “Scalar and pseudoscalar Higgs production in association with a
 996 top-antitop pair”, *Phys.Lett.* **B701** (2011) 427–433,
 997 doi:[10.1016/j.physletb.2011.06.012](https://doi.org/10.1016/j.physletb.2011.06.012), [arXiv:1104.5613](https://arxiv.org/abs/1104.5613).
- 998 [33] M. Garzelli, A. Kardos, C. Papadopoulos, and Z. Trocsanyi, “Standard Model Higgs boson
 999 production in association with a top anti-top pair at NLO with parton showering”,
 1000 *Europhys.Lett.* **96** (2011) 11001, doi:[10.1209/0295-5075/96/11001](https://doi.org/10.1209/0295-5075/96/11001), [arXiv:1108.0387](https://arxiv.org/abs/1108.0387).

- 1001 [34] S. Dawson, L. Orr, L. Reina, and D. Wackerlo, “Associated top quark Higgs boson
 1002 production at the LHC”, *Phys.Rev.* **D67** (2003) 071503,
 1003 [doi:10.1103/PhysRevD.67.071503](https://doi.org/10.1103/PhysRevD.67.071503), [arXiv:hep-ph/0211438](https://arxiv.org/abs/hep-ph/0211438).
- 1004 [35] T. Gleisberg et al., “Event generation with SHERPA 1.1”, *JHEP* **0902** (2009) 007,
 1005 [doi:10.1088/1126-6708/2009/02/007](https://doi.org/10.1088/1126-6708/2009/02/007), [arXiv:0811.4622](https://arxiv.org/abs/0811.4622).
- 1006 [36] P. Artoisenet, R. Frederix, O. Mattelaer, and R. Rietkerk, “Automatic spin-entangled
 1007 decays of heavy resonances in Monte Carlo simulations”, *JHEP* **1303** (2013) 015,
 1008 [doi:10.1007/JHEP03\(2013\)015](https://doi.org/10.1007/JHEP03(2013)015), [arXiv:1212.3460](https://arxiv.org/abs/1212.3460).
- 1009 [37] F. Cascioli, P. Maierhofer, and S. Pozzorini, “Scattering Amplitudes with Open Loops”,
 1010 *Phys.Rev.Lett.* **108** (2012) 111601, [doi:10.1103/PhysRevLett.108.111601](https://doi.org/10.1103/PhysRevLett.108.111601),
 1011 [arXiv:1111.5206](https://arxiv.org/abs/1111.5206).
- 1012 [38] F. Krauss, R. Kuhn, and G. Soff, “AMEGIC++ 1.0: A Matrix element generator in
 1013 C++”, *JHEP* **0202** (2002) 044, [doi:10.1088/1126-6708/2002/02/044](https://doi.org/10.1088/1126-6708/2002/02/044),
 1014 [arXiv:hep-ph/0109036](https://arxiv.org/abs/hep-ph/0109036).
- 1015 [39] T. Gleisberg and F. Krauss, “Automating dipole subtraction for QCD NLO calculations”,
 1016 *Eur.Phys.J.* **C53** (2008) 501–523, [doi:10.1140/epjc/s10052-007-0495-0](https://doi.org/10.1140/epjc/s10052-007-0495-0),
 1017 [arXiv:0709.2881](https://arxiv.org/abs/0709.2881).
- 1018 [40] Planck Collaboration, “Planck 2013 results. I. Overview of products and scientific results”,
 1019 *Astron.Astrophys.* **571** (2014) A1, [doi:10.1051/0004-6361/201321529](https://doi.org/10.1051/0004-6361/201321529),
 1020 [arXiv:1303.5062](https://arxiv.org/abs/1303.5062).
- 1021 [41] V. Rubin, N. Thonnard, and J. Ford, W.K., “Rotational properties of 21 SC galaxies with
 1022 a large range of luminosities and radii, from NGC 4605 /R = 4kpc/ to UGC 2885 /R =
 1023 122 kpc/”, *Astrophys.J.* **238** (1980) 471, [doi:10.1086/158003](https://doi.org/10.1086/158003).
- 1024 [42] Super-Kamiokande Collaboration Collaboration, “Measurements of the solar neutrino flux
 1025 from Super-Kamiokande’s first 300 days”, *Phys.Rev.Lett.* **81** (1998) 1158–1162,
 1026 [doi:10.1103/PhysRevLett.81.1158](https://doi.org/10.1103/PhysRevLett.81.1158), [arXiv:hep-ex/9805021](https://arxiv.org/abs/hep-ex/9805021).
- 1027 [43] KamLAND Collaboration Collaboration, “Measurement of neutrino oscillation with
 1028 KamLAND: Evidence of spectral distortion”, *Phys.Rev.Lett.* **94** (2005) 081801,
 1029 [doi:10.1103/PhysRevLett.94.081801](https://doi.org/10.1103/PhysRevLett.94.081801), [arXiv:hep-ex/0406035](https://arxiv.org/abs/hep-ex/0406035).
- 1030 [44] MINOS Collaboration Collaboration, “Observation of muon neutrino disappearance with
 1031 the MINOS detectors and the NuMI neutrino beam”, *Phys.Rev.Lett.* **97** (2006) 191801,
 1032 [doi:10.1103/PhysRevLett.97.191801](https://doi.org/10.1103/PhysRevLett.97.191801), [arXiv:hep-ex/0607088](https://arxiv.org/abs/hep-ex/0607088).

- [45] S. P. Martin, “A Supersymmetry primer”, *Adv.Ser.Direct.High Energy Phys.* **21** (2010) 1–153, doi:10.1142/9789814307505_0001, arXiv:hep-ph/9709356.
- [46] J. Aguilar-Saavedra, R. Benbrik, S. Heinemeyer, and M. Prez-Victoria, “Handbook of vectorlike quarks: Mixing and single production”, *Phys.Rev.* **D88** (2013), no. 9, 094010, doi:10.1103/PhysRevD.88.094010, arXiv:1306.0572.
- [47] G. Burdman, M. Perelstein, and A. Pierce, “Large Hadron Collider tests of a little Higgs model”, *Phys.Rev.Lett.* **90** (2003) 241802, doi:10.1103/PhysRevLett.90.241802, arXiv:hep-ph/0212228.
- [48] M. Perelstein, M. E. Peskin, and A. Pierce, “Top quarks and electroweak symmetry breaking in little Higgs models”, *Phys.Rev.* **D69** (2004) 075002, doi:10.1103/PhysRevD.69.075002, arXiv:hep-ph/0310039.
- [49] H.-C. Cheng, I. Low, and L.-T. Wang, “Top partners in little Higgs theories with T parity”, *Phys. Rev. D* **74** (Sep, 2006) 055001, doi:10.1103/PhysRevD.74.055001.
- [50] H.-C. Cheng, B. A. Dobrescu, and C. T. Hill, “Electroweak symmetry breaking and extra dimensions”, *Nucl.Phys.* **B589** (2000) 249–268, doi:10.1016/S0550-3213(00)00401-6, arXiv:hep-ph/9912343.
- [51] M. S. Carena, E. Ponton, J. Santiago, and C. E. Wagner, “Light Kaluza Klein States in Randall-Sundrum Models with Custodial SU(2)”, *Nucl.Phys.* **B759** (2006) 202–227, doi:10.1016/j.nuclphysb.2006.10.012, arXiv:hep-ph/0607106.
- [52] C. T. Hill, “Topcolor: Top quark condensation in a gauge extension of the standard model”, *Phys.Lett.* **B266** (1991) 419–424, doi:10.1016/0370-2693(91)91061-Y.
- [53] R. Contino, L. Da Rold, and A. Pomarol, “Light custodians in natural composite Higgs models”, *Phys.Rev.* **D75** (2007) 055014, doi:10.1103/PhysRevD.75.055014, arXiv:hep-ph/0612048.
- [54] L. Evans and P. Bryant, “LHC Machine”, *JINST* **3** (2008) S08001, doi:10.1088/1748-0221/3/08/S08001.
- [55] M. Benedikt et al., “LHC Design Report Vol3 - The Injection Chain”. CERN, Geneva, 2004.
- [56] C. Hill et al., “Tests of the CERN proton linac performance for LHC - type beams”, *eConf* **C000821** (2000) TUD17, arXiv:physics/0008102.
- [57] K. S. Klaus Hanke, and Michel Chanel.

- 1064 [58] “Image, CERN PSbooster Layout”.
1065 URL <http://psb-machine.web.cern.ch/psb-machine/>.
- 1066 [59] S. Baird, “Accelerators for pedestrians; rev. version”, Technical Report AB-Note-2007-014.
1067 CERN-AB-Note-2007-014. PS-OP-Note-95-17-Rev-2. CERN-PS-OP-Note-95-17-Rev-2,
1068 CERN, Geneva, Feb, 2007.
- 1069 [60] “CERN Website, Super Proton Synchrotron”.
1070 URL <http://home.web.cern.ch/about/accelerators/super-proton-synchrotron>.
- 1071 [61] G. Dme, “The SPS acceleration system travelling wave drift-tube structure for the CERN
1072 SPS”, .
- 1073 [62] O. S. Brning et al., “LHC Design Report Vol1 - The Main Ring”. CERN, Geneva, 2004.
- 1074 [63] “CERN, List of All LHC Magnets”. URL http://lhc-machine-outreach.web.cern.ch/lhc-machine-outreach/components/magnets/types_of_magnets.htm.
- 1075 [64] M. Barnes, J. Borburgh, B. Goddard, and M. Hourican, “Injection and extraction
1076 magnets: septa”, [arXiv:1103.1062](https://arxiv.org/abs/1103.1062).
- 1077 [65] M. Barnes et al., “Injection and extraction magnets: Kicker magnets”, [arXiv:1103.1583](https://arxiv.org/abs/1103.1583).
- 1078 [66] “Outreach, CERN LHC, Cryogenic System”. URL <http://home.web.cern.ch/about/engineering/cryogenics-low-temperatures-high-performance>.
- 1079 [67] “The challenge of keeping cool”, .
- 1080 [68] P. Lebrun, “Large Cryogenic Helium Refrigeration System for the LHC”, Technical
1081 Report LHC-Project-Report-629. CERN-LHC-Project-Report-629, CERN, Geneva, Feb,
1082 2003. revised version number 1 submitted on 2003-02-19 11:44:11.
- 1083 [69] “Outreach, CERN LHC, Vacuum System”. URL <http://home.web.cern.ch/about/engineering/vacuum-empty-interplanetary-space>.
- 1084

¹⁰⁸⁷ List of Acronyms

¹⁰⁸⁸ **ATLAS** A Toroidal LHC Apparatus

¹⁰⁸⁹ **BSM** Beyond the Standard Model

¹⁰⁹⁰ **CERN** European Center for Nuclear Research

¹⁰⁹¹ **CMS** Compact Muon Solenoid

¹⁰⁹² **FSR** Final State Radiation

¹⁰⁹³ **ISR** Initial State Radiation

¹⁰⁹⁴ **JHEP** Journal of High Energy Physics

¹⁰⁹⁵ **LHC** Large Hadron Collider

¹⁰⁹⁶ **LO** Leading Order

¹⁰⁹⁷ **MVA** Multi-Variate Analysis

¹⁰⁹⁸ **NLO** Next to Leading Order

¹⁰⁹⁹ **QCD** Quantum Chromodynamics

¹¹⁰⁰ **QED** Quantum Electrodynamics

¹¹⁰¹ **QFT** Quantum Field Theory

¹¹⁰² **SM** Standard Model